The Pennsylvania State University

The Graduate School

College of Engineering

ONLINE DISCONTINUITY DETECTION IN METALLIC POWDER BED FUSION ADDITIVE MANUFACTURING PROCESSES USING VISUAL INSPECTION SENSORS AND SUPERVISED MACHINE LEARNING

A Thesis in

Mechanical Engineering

by

Christian Gobert

Submitted in Partial Fulfillment
of the Requirements
for the Degree of

Master of Science

May 2017

The thesis of Christian Gobert was reviewed and approved* by the following:

Asok Ray
Professor of Mechanical Engineering and Mathematics
Thesis Advisor

Shashi Phoha
Senior Research Associate at Applied Research Lab
Graduate Faculty Department of Electrical Engineering

Edward Reutzel
Associate Professor of Engineering Science and Mechanics, Graduate Faculty

Jan Petrich
Technical Advisor, R&D Engineer at Applied Research Lab

Guha Prasanna Manogharan
Assistant Professor of Mechanical Engineering

Karen Thole
Distinguished Professor of Mechanical Engineering
Department Head of Mechanical Engineering

*Signatures are on file in the Graduate School.

ABSTRACT

Additive manufacturing (AM) has garnered appeal as having the potential to provide cost-savings for high-end low-volume parts, to enable cost-effective consolidated and complex part designs for enhanced performance, and to make supply-chain management operations more efficient. Certifying adequate part quality remains a barrier to implementation, and process monitoring and part qualification during metallic AM processes may serve as a crucial enabler for the widespread adoption of metallic AM in industrial, military and commercial settings. Post build evaluation techniques, such as x-ray computerized tomography (CT), can identify discontinuities in AM parts, however post-build inspection is costly, and embedded defects may be difficult or impossible to repair. The layerwise construction of metallic powder bed fusion AM(PBFAM) parts presents the opportunity to repair defects during the build process, and so the ability to detect flaws in situ could enable cost-effective in-process re-melting and correction of detected flaws in AM parts. High resolution imaging of build layers may provide a cost-effective means to realize in situ flaw detection, compared to melt pool monitoring and post-build evaluation techniques, to achieve in-process certification. This research investigates and explores a discontinuity detection scheme implemented in a metallic PBFAM system using supervised machine learning on sensor data collected in situ during each layer of the AM build process. A PBFAM system was instrumented with a high resolution digital single lens reflex (DSLR) camera that captured multiple images of the entire build platform following each powder recoating and laser fusion step of each layer in the build. Ground truth labels defining part condition, e.g. anomalous or nominal, were extracted from post-build high resolution CT scans of a single AM part utilizing advanced image processing tools. The anomalous

features detected within the CT scan were manually verified to correspond to discontinuities within the component, and were depicted in a 3D representation to provide insight into the development of part flaws during the build process. An affine transformation was generated to map the CT scan data and 3D location of discontinuities into the DSLR layerwise image data using reference points in the AM part, enabling the definition of anomalous and nominal ground truth labels of discretized locations obtained from CT scan data to be properly located within the DSLR layerwise images. Based on knowledge of the AM process and the accuracy of the generated affine transformation, multi-dimensional features were extracted from labeled anomalous and nominal DSLR image locations. Supervised machine learning was employed to study the severability of the labeled anomalous and nominal features directly within the domain of the in situ layerwise images. Linear support vector machine (SVM) models were used to create two discontinuity detection strategies, which were then validated through four-fold cross-validation. Both detection strategies were (i) evaluated with several performance metrics and assessed with respect to discontinuity size, (ii) validated by identifying similar discriminatory separation between cross-validated models, and (iii) evaluated with the presence of sensor noise added to the DSLR layerwise images.

TABLE OF CONTENTS

LIST OF FIGURES vii
LIST OF TABLES x
NOMENCLATURE xi
ACKNOWLEDGEMNTS xiv
CHAPTER 1 Introduction 1
1.1 Additive Manufacturing 1
1.1.1 Introduction to AM and PBFAM 1
1.1.2 Impact and Application of AM 2
1.2 Literature Review for Process Monitoring 3
1.2.1 Part Quality 3
1.2.2 Process Monitoring 4
1.3 Research Objectives 6
CHAPTER 2 Experimental Setup and Procedure 8
2.1 Camera Setup 8
2.2 AM System Settings 8
2.3 Test Part Design 9
2.4 Data Collection 10
2.4.1 DSLR Image Data 10
2.4.2 CT Data 12
2.4.3 AM System Data 13
CHAPTER 3 Ground Truth Labeling 15
3.1 Identifying Anomalous and Nominal CT Voxels 15
3.1.1 Defining Anomaly and Nominal CT Voxels 15
3.1.2 Locating with Convolution Operations 15
3.1.3 Locating Anomalous CT Voxels 17
3.1.4 Locating Nominal CT Voxels 18
3.2 Labeling and Clustering Anomaly CT Voxels 19
3.2.1 Clustering Strategy and Implementation for Anomaly CT Voxels 19
3.2.2 Initial Screening of Anomaly CT Voxels 19
3.2.3 K-Means Clustering of Anomaly CT Voxels 21
3.2.4 Further Anomaly CT Cluster Screening 23
3.3 Examination of Ground Truth Labels 27

3.3.1 Anomaly and Nominal CT Voxels 27
3.3.2 Anomaly CT Clusters 27
CHAPTER 4 DSLR Domain Ground Truth Labeling and Feature Extraction 31
4.1 Ground Truth Labeling the DSLR Domain from the CT Domain 31
4.1.1 Need for Coordinate Transformation 31
4.1.2 Extracting Reference Points 31
4.1.3 Coordinate Transformation 31
4.2 Feature Extraction from DSLR Flash Module Image Stacks 37
4.2.1 Linking Coordinate Transformation to Feature Extraction 37
4.2.2 Defining Feature Extraction Filter Size 39
4.2.3 Feature Extraction 41
4.2.4 Sample Size for Discontinuity Detection 42
4.3 Examination of Nominal and Anomaly DSLR Labels and Images 43
CHAPTER 5 Machine Learning in PBFAM Discontinuity Detection 46
5.1 Methodology of SVMs in Discontinuity Detection 46
5.2 SVMs, Ensemble Classification, and Performance Analysis 47
5.2.1 SVMs 47
5.2.2 Ensemble Classification with SVMs 50
5.2.3 Cross-validation and Performance Evaluation 51
5.3 Evaluation of SVM Ensemble Discontinuity Detection 54
5.3.1 Ensemble Model Performance 54
5.3.2 Robust Analysis of Ensemble Model 61
5.4 Evaluation of Single SVM Discontinuity Detection 62
5.4.1 Single SVM Model Performance and Validation 62
5.4.2 Robust Analysis of Single SVM Model 66
CHAPTER 6 CONCLUSION 67
6.1 Assessment of Discontinuity Detection Scheme 67
6.2 Improvements and future work 69
References 72
Appendix A. CT and DSLR 3Images of an Anomaly Sample 75
Appendix B. CT and DSLR Images of a Nominal Sample 77

LIST OF FIGURES

Figure 2.1. Location of camera system and light sources within the build chamber. (1) - (8) sequence and locations of flash modules. 9

Figure 2.2 3D CAD model of step cylinder. Step 1 and step 23 reference points are shown. 10

Figure 2.3 DSLR image of the entire build plate from flash module 6. 11

Figure 2.4 Eight flash module images of step 23: (1)-(3) post powder recoating flash modules and (4)-(8) post fusion flash modules. 12

Figure 2.5 CT image layer from step 23.....13

Figure 2.6 Slicing data image of step 23 14

Figure 3.1 Gabor filter with S=11 and $\sigma g = 1$. 17

Figure 3.2 CT image (left) and kernel response image (right) of a pore anomaly CT voxel (centered in each image).....20

Figure 3.3 Exclusive cluster assignments with respect to number of k-mean clusters for pore anomaly CT voxels.....23

Figure 3.4 An anomaly CT clusters made up of two individual neighborhoods of CT anomaly voxels and outlined occupational volume (in blue) of anomaly CT cluster. 24

Figure 3.5 The anomaly CT cluster shown in figure 3.4 is split into two individual CT clusters whose packing ratio is now 0.312 and 0.199 respectively. 26

Figure 3.6 An anomaly CT cluster which was not split. 26

Figure 3.7 Anomaly and nominal CT voxel in CT image (left) and S = 11 Gabor filter Response (right). 27

Figure 3.8 CT scan view of an anomaly CT 28

Figure 3.9 Frequency of CT cluster class size (blue – left axis) and total number of CT voxels per class (green – right axis). 29

Figure 3.10 Location of all discovered anomaly CT clusters in the SLI domain within the transparent cylinder shown in front, side, top and isometric view. 30

Figure 4.1 CT voxel compared to DSLR voxel. 33

Figure 4.2 Observed and transformed reference points in flash module 1 domain. 33

Figure 4.3 Histogram of reference point coordinate transformation error in the DSLR flash module 1 domain for the x, y and z axis. 34

Figure 4.4 Frequency of DSLR cluster size class (blue – left axis) and total number of DSLR voxels (green – right axis) per class. 36

Figure 4.5 Coordinate transformation of red outlined region from the CT domain (pictured left) into flash module 3 image stack (pictured right). 37

Figure 4.6 Outline of feature extraction filter over a ground truth anomaly in two DSLR flash module domains. 41

Figure 4.7 Anomaly label depicted in three builds layers of two flash modules and CT image with the respective feature extraction filter in red 44

Figure 4.8 Nominal label depicted in three builds layers of two flash modules and CT image with the respective feature extraction filter in red 45

Figure 5.1 Example of separating hyperplanes as part of a SVM. (Source [36]) 48

Figure 5.2 Ensemble Classification Scheme. 51

Figure 5.3 Flash module 6 image (left) with added noise at P = 30 (right). 54

Figure 5.4 Frequency of condition positive (blue – left axis) and true positive (green – right axis) DSLR anomalies with respect to DSLR cluster size for ensemble classification. 56

Figure 5.5 Frequency of cluster size (blue – left axis) and detected clusters (green - right axis) per DSLR cluster size of the ensemble classifier. 57

Figure 5.6 Standardized signed distance to hyperplane values for the ensemble SVM classifier. 58

Figure 5.7 ROC curve for ensemble classifier cross-validated models. 59

Figure 5.8 Robust analysis of ensemble SVM discontinuity detection strategy displaying range of metric values for each value of P. 61

Figure 5.9 Frequency of condition positive (blue – left axis) and true positive (green – right axis) DSLR anomalies with respect to DSLR cluster size of the single SVM. 63

Figure 5.10 Frequency of cluster size (blue – left axis) and detected clusters (green – right axis) per DSLR cluster size of the single SVM. 63

Figure 5.11 Standardized signed distance to hyperplane values for single SVM cross-validated models. 65

Figure 5.12 ROC curve for single SVM classifier cross-validated models. 65

Figure 5.13 Robust analysis of single SVM discontinuity detection strategy displaying range of metric values for each value of P. 66

Figure A.1 CT images of anomaly sample with red outline representing feature extraction filter from DSLR domain 75

Figure A.2 Flash module 1-4 images of anomaly sample from previous, current and following build layer (depicted in figure A. 1) with outline of feature extraction filter in red. 75

Figure A.3 Flash module 5-8 images of anomaly sample from previous, current and following build layer (depicted in figure A. 1) with outline of feature extraction filter in red. 76

Figure B.1 CT images of nominal sample with red outline representing feature extraction filter from DSLR domain 77

Figure B.2 Flash module 5-8 images of anomaly sample from previous, current and following build layer (depicted in Figure A – 2) with outline of feature extraction filter in red. 77

Figure B.3 Flash module 5-8 images of nominal sample from previous, current and following build layer (depicted in Figure A – 2) with outline of feature extraction filter in red. 78

LIST OF TABLES

Table 4.1 Flash Shift of DSLR modules with respect to DSLR flash module 1.....35

Table 4.2 Displacement (DSLR voxels) to anomaly cluster centroid for anomaly DSLR voxels. 36

Table 5.1 Average value and standard deviations of accuracy, precision and recall for each feature matrix SVM classifier and ensemble classifier……..55

Table 5.2 Ensemble classification recall with respect to voxel displacement to anomaly cluster centroid.....58

Table 5.3 SVM model parameters from ensemble cross-validation. 60

Table 5.4 Performance metrics for the ensemble classifier and single SVM classifier. ...62

Table 5.5 Single SVM classification recall with respect to voxel displacement to anomaly cluster centroid.....64

NOMENCLATURE

AM	Additive Manufacturing
CAD	Computer-Aided Design
STL	Standard Tessellation Language
PBFAM	Powder Bed Fusion Additive Manufacturing
CT	Computed Tomography
CCD	Charged Coupled Device
IR	Infrared
SVM	Support Vector Machine
DSLR	Digital Single-Lens Reflex
I_f	DSLR voxel intensity
x_I	Voxel Row Location
y_I	Voxel Column Location
z_I	Voxel Layer Location
f_I	DSLR Voxel Location Flash Index in I_f
I_{CT}	CT Voxel Intensity
x_{CT}	Voxel Row Location
y_{CT}	Voxel Column Location
z_{CT}	Voxel Layer Location
G_{3D}	3D Gabor filter
x_g	X Cartesian Coordinate of G_{3D}
y_g	Y Cartesian Coordinate of G_{3D}
z_g	Z Cartesian Coordinate of G_{3D}
σ_g	Standard deviation of Underlying Gaussian Envelope
r_g	Distance to Center of Gabor Filter
Z	Domain of x_g, y_g and z_g
S	Size of G_{3D}
g_a	Standard Deviation Threshold for Anomaly Detection
Ap_r	Anomaly Pore CT Voxel Matrix
As_r	Anomaly Super-Density CT Voxel Matrix

n_s	Number of Anomaly Super-Density CT Voxels in A_s
n_p	Number of Anomaly Pore CT Voxels in A_p
g_n	Standard Deviation Threshold for Nominal Detection
N_n	Nominal CT Voxel Matrix
n_n	Number of Nominal CT voxels in N_n
n_{CT}	Minimum Number of Neighboring Anomaly CT Voxels
d_v	Threshold Distance for Neighboring Anomaly CT Voxels
A_{pt}	Initial Screened Anomaly Pore Matrix
A_{st}	Initial Screened Anomaly Super-density Matrix
n_{pt}	Reduced n_p After Initial Screening
n_{st}	Reduced n_s After Initial Screening
k_d	Exclusive Cluster Assignment Threshold Radius
k	Imposed Number of K-Means Clusters
k_{maxp}	Maximum Number of Imposed Clusters
k_c	k with Greatest Number of Exclusive Cluster Assignment
PR	Packing Ratio
T_{CT}	True Volume of Anomaly CT Cluster
L_{CT}	Length of Anomaly CT Cluster
H_{CT}	Height of Anomaly CT Cluster
W_{CT}	Width of Anomaly CT Cluster
RSME	Root Mean Square Error
RMSE_x	Root Mean Square Error in X direction
RMSE_y	Root Mean Square Error in Y direction
RMSE_z	Root Mean Square Error in Z direction
x_j	X Coordinate of Observed Reference Points
y_j	Y Coordinate of Observed Reference Points
z_j	Z Coordinate of Observed Reference Points
n_r	Number of Reference Points
$\hat{x}_j$	X Coordinate of Transformed Reference Points
$\hat{y}_j$	Y Coordinate of Transformed Reference Points

$\hat{z}_j$	Z Coordinate of Transformed Reference Points
L_s	Number of Standard Deviations for Feature Extraction Filter
x_f	DSLR Voxel Length (X Cartesian axis) of Feature Extraction Filter
y_f	DSLR Voxel Width (Y Cartesian axis) of Feature Extraction Filter
z_f	DSLR Voxel Height (Z Cartesian axis) of Feature Extraction Filter
n_{total}	Total Number of DSLR Voxel Samples for Discontinuity Detection
F_n	Number of Linearly-Independent Feature Dimensions
M_f	Feature Matrix with index f
f	Flash Module Number
V	Number of Flash Module Image Stacks
$\vec{x}_{fi}$	Feature Vectors of Samples
y_i	Class Labels
$\overrightarrow{w_f}$	Flash Module SVM Normal Vector to Hyperplane
b_f	Flash Module SVM Bias
$\vec{x}$	Support Vectors
λ	Box Constraint
$d(\vec{x}_{fi})$	Distance to Hyperplane for f Flash Module SVM
$\overrightarrow{w_s}^T$	Single SVM Normal Vector
b_s	Single SVM Bias
F_E	Ensemble Feature Matrix
$\vec{e}_i$	Vector of Ensemble Feature Space
P	Pixel Intensity Value
$\overrightarrow{w_e}$	Ensemble SVM Normal Vector
b_e	Ensemble SVM Bias

ACKNOWLEDGEMNTS

I would like to first thank my thesis advisor Dr. Asok Ray for his guidance and help along my thesis work. I would also like to thank Dr. Shashi Phoha for her support of this project. I would like to thank Dr. Ted Reutzel for his insight and enthusiasm. I would like to thank Dr. Jan Petrich for his continually effort and guidance during the entirety of my research and work. I would like to Dr. Guha Prasanna Manogharan for his help on this thesis.

This work would not have been possible without the contributions of several individuals and organizations. I would like to thank Naval Air Systems Command for their support. I would like to thank Dr. Abdalla Nassar for help on this research and experiment design. I would like to thank Ms. Gabrielle Gunderman and Mr. Griffin Jones, from ARL Penn State for their efforts designing the experiments and for performing post-process inspection via 3D computed tomography analysis. Finally, I wish to thank Mr. Don Natale, Mr. Jacob Morgan, and Mr. John Morgan for their contributions in the area of imaging system design and calibration, and for their contributions to the design of the test artifact.

This material is based, in part, upon work supported by the Naval Air Systems Command (NAVAIR) under Contract No. N00024-12-D-6404, Delivery Order 0321 and also by support from the Applied Research Laboratory at the Pennsylvania State University. Any opinions, findings and conclusions or recommendations expressed in this material are those of the author and do not necessarily reflect the views of the Naval Air Systems Command (NAVAIR)

CHAPTER 1 Introduction

1.1 Additive Manufacturing

1.1.1 Introduction to AM and PBFAM

Additive manufacturing (AM) is a process in which near-net-shape parts are built directly from digital files in a layerwise manner, in contrast to conventional subtractive and formative manufacturing techniques [1]. AM loosely follows an eight-step process in order of: computer-aided design (CAD) solid model creation, standard tessellation language (STL) file format conversion, file transfer to AM machine, AM build, removal from AM machine, post-process, and treatment [2].

Metallic laser powder bed fusion AM (PBFAM) is a form of AM in which a focused laser beam selectively melts metal powder atop the build platform (i.e. metallic substrate) inside a build chamber, fusing the metal powders in consecutive layers to form a 3D part. [1]. A melt pool forms where the laser beam interacts with the metal powders, and the impinging energy from the laser beam is sufficient to melt the powder and re-melt portions of previous solidified layers. The build chamber is an enclosed space, typically filled with an inert gas, where parts are fabricated and where the build platform serves as a substrate for initiating a build [1]. In metallic PBFAM, a layer of metal powder is spread across the build platform after it is lowered an amount corresponding to the layer thickness. A recoater blade, rake or roller spreads the metal powder across the build platform from an adjacent powder reservoir. Depending on part dimensions, material and customer specifications PBFAM parts are made up of hundreds or thousands of layers (typically ~20-60 μm layer thickness) with build times range from hours to days [3].

In PBFAM studies, a simplified energy density equation has been used to correlate process parameters as a metric for comparing and characterizing builds. Energy density is a function of laser power, scan velocity (speed of the laser), and scan spacing or hatch distance (spacing between parallel laser paths) [2]. The melt pool size, depth and thermal history are a function of process parameters, including irradiance and absorbed energy, and melt pool behavior has a considerable effect on part quality [4].

1.1.2 Impact and Application of AM

Advantages of AM over conventional manufacturing techniques include: elimination of tooling, cost-effective production of small lots, optimization and customization of product design (including consolidation of parts), simplification of supply chains, reduction of material waste and production of complex part geometries [5-8]. Khajavi *et al.* studied the effect of polymer-based AM on a spare parts supply chain for the F-18 Super Hornet [9], being one of the earliest and most documented deployments of AM technology. Employing AM in a distributed production strategy potentially provides lower operation costs, lower capacity utilization, and higher robustness to supply chain disruptions. AM can serve in a rapid tooling role in conjunction with other manufacturing techniques, producing molds to reduce time and cost for development, where AM cannot directly compete with the associated low cost and high production volume of conventional manufacturing techniques [10]. In the biomedical field, AM has been used to produce custom-shaped orthopedic prostheses and implants for patients [2]. AM can impact smaller businesses and end-users by enabling the operators, themselves, to serve as self-sufficient designers and manufacturers in order to develop, design and produce products on their own, thereby lowering the entry-barrier to manufacturing [3].

1.2 Literature Review for Process Monitoring

1.2.1 Part Quality

Part porosity in PBFAM is common, and such porosity negatively affects the mechanical properties of AM parts. Studies suggest formation of voids during PBFAM can be powder-induced (i.e. irregularities in powder recoating), process-induced (i.e. laser-material interaction) or as a result of part solidification (i.e. high thermal gradients across the part subject to cooling) [11-14]. Additionally, porosity can form from entrapped gas pores, appearing spherical in shape and with diameters in the order of ten of microns, or from elongated voids, arising from a lack of fusion between powder particles that can extend to several hundred microns in length [15]. Gong *et al.* [16] and Thijs *et al.* [17] studied the effect of energy density on AM part porosity, finding that "over-melting" results in subsurface discontinuities such as gas pores, whereas "fully dense" and "incomplete melting" results in void discontinuities visible on the part surface.

Part quality can be confirmed and inspected in various post-process analyses (i.e. after the build is complete and part removed from the build plate) via Archimedes method, micrography and X-ray scanning [18]. X-ray scanning by means of 3D computerized tomography (CT) is a non-destructive evaluation technique providing information on part geometry and enabling the identification of discontinuities within a part [19]. Both Spearings *et al.* [18] and Wits *et al.* [19] demonstrated that Archimedes, micrography and CT methods predict similar densities of identical parts. Archimedes method can only report the average density of an object; while micrography is a destructive and time consuming post evaluation process that only provides information from a single 2D plane. CT scanning for the detection of porosities is subject to size detection thresholds and so-called

"shadowing" from irregular part geometry, but it enables part porosity to be quantified and precisely located in three-dimensional space, a critical feature to enable supervised machine learning.

1.2.2 Process Monitoring

Research in AM, specifically for process monitoring, has seen a significant increase in the past decade driven by the appeal of AM [20]. Attention to process monitoring has increased due to the inherent variability between AM systems and resulting variability in part quality which limits the widespread adoption of AM [21]. Traditional statistics-based quality control used for high volume production is not effective at quality control in AM, typically implemented for low volume production. Using post process analysis techniques to grade part quality can be expensive and detection of discontinuities post-process ultimately limits repair strategies. If process monitoring technology can assess part quality *during* the build process it may enable corrective action to be taken during the build process to ensure optimum part quality [22].

Melt-pool process monitoring can provide great insight into part quality and process phenomena as melt-pool dynamics have a significant role in part quality. As a consequence, temperature monitoring in PBF represents a majority of process monitoring research in metal-based AM [20]. However, melt-pool monitoring requires tight integration within an AM system, which is expensive and limits the adoption of a developed process monitoring system if tailored to a specific AM system. Additionally, analysis of melt-pool dynamics can be complicated due to challenges in extremely high data rates required for high speed imaging, emissivity calibration of melt pools and investment of costly equipment [20]. Online process monitoring using more conventional imaging sensors (i.e. digital cameras)

in a system-independent and inexpensive approach relative to melt-pool process monitoring [20].

Kleszczynski *et al.* [23] demonstrated the implementation of a system-independent-imaging system using a 29-megapixel charge coupled device (CCD) camera for a PBFAM process which captured *in situ* images of the build plate, one image after powder deposition and laser beam melting where the light source was always perpendicular to the current powder bead orientation. Parts were built with inadequate process conditions, such as enlarged hatch distance, contaminated powder, poor support structures and high energy input, which were then characterized using the *in situ* layerwise images taken. Jacobsmuhlen *et al.* [24] advance this work by using image processing on *in situ* layerwise images during powder recoating to detect so-called *super-elevated* regions during the build, which would tend to induce process errors (i.e. recoater blade and part collision). Parts with induced errors were subsequently mechanically tested to build a connection between process parameters, layerwise surface images, and mechanical properties. Mireles *et al.* [25] presented a 0.3-megapixel infrared (IR)-layerwise imaging system on an electron beam-based PBFAM process to observe seeded void discontinuities in parts, seeded voids ranged in size from 100 µm to 2 mm in diameter. Geometries of porous discontinuities were measured with contour tracing in the IR-layerwise and CT images. A formal comparison revealed that a substantial difference of measured geometry existed between the two domains, roughly 53% in measured geometries of voids. Additionally, Mireles *et al.* demonstrated efficacy of *in situ* correction strategies using re-melting of the defective area for seeded defects locally identified with a 0.3-megapixel IR-camera in an AM part, seeded defects below 600 µm were not detected by the IR camera or not properly fabricated

by the EBM system; correction of located seeded defects entailed layer re-melting. Schwerdtfeger *et al.* [26] demonstrated a correspondence between low-resolution IR-layerwise imaging and metallographic imaging of electron-beam-based PBFAM parts. Aminzadeh *et al.* [27] proposed detection of flaws in PBFAM parts using online visual inspection sensors, in varying sensor configurations, paired with classifiers, potentially neural networks or support vector machines (SVMs), but did not report any details or results.

1.3 Research Objectives

This investigation is built upon the hypothesis that visual process sensors monitoring a PBFAM process, specifically high resolution *in situ* imaging of build surfaces, can capture visible features on build surfaces of individual layers during a PBFAM build that can be linked discontinuities or indications of discontinuities in the resultant component. Then using post-process CT part scans, a linear SVM machine learning model can be trained and supervised to use layerwise images of build surfaces, alone, to detect part flaws. This thesis explores the development and implementation of a discontinuity detection methodology in a metallic PBFAM process using visual inspection sensors, data fusion, and supervised machine learning to detect discontinuities arising from process errors in a nominal build environment. Specific contributions include:

- labeling the binary ground truth of part regions as either discontinuities or fully-dense in a PBFAM part using automated image processing techniques on post-build CT imaging
- transferring ground truth labels identified in CT images into *in situ* visual data domains

- extracting labeled information from *in situ* visual data domains for supervised machine learning and discontinuity detection
- generating two supervised classification methodologies using linear SVM binary classifiers to classify labeled anomalous and nominal regions using *in situ* visual data
- evaluating performance of generated discontinuity detection methodologies under cross validation studies
- assessing the achievable robustness to sensor noise of discontinuity detection

CHAPTER 2 Experimental Setup and Procedure

2.1 Camera Setup

A PBFAM build process conducted in an EOS M280 AM system [28] was monitored by a 36.3-megapixel digital single-lens reflex (DSLR) CCD camera (Nikon D800E) mounted inside the build chamber. The DSLR camera captured a total of eight images of the build platform using five light sources for each build layer, with each different condition designated as a flash module. The set-up is illustrated in figure 2.1, with each number next to a light source indicating the designated flash module, with some light sources employed both after powder recoating operation and again after the laser fusion step. The variation in lighting angle and characteristics enhances contrast in different ways, and reveals additional information that could not be provided by a single lighting source alone. The additional lighting sources added to the system were covered with several layers of light-diffusing film. Timing of image capture was triggered via proximity-sensor monitoring of the recoater blade, with images (1) - (3) captured immediately following the powder recoating operation, images (4) - (8) were captured immediately following the laser fusion step. Additional details concerning the camera and light system setup in the EOS M280 AM system are reported in [29].

2.2 AM System Settings

For this investigation, the EOS M280 system settings were set to EOS standard conditions, which can be expected to result in a minimal number of discontinuities or indications, with most regions of the component free of voids and therefore suitable to be labeled as nominal (i.e. fully dense) conditions. This approach for the AM system settings was used to create an environment which produced relatively few anomalous regions, i.e.

with isolated discontinuities or indications, which could be easily compared against nominal conditions, i.e. indication-free regions of the part. A PBFAM part created in this setting would be comparable to a real-world application where so-called optimal process parameters would be used in an attempt to limit the formation of part flaws. Process parameter settings of the EOS M280 system for this investigation included: hatch distance at 0.1 mm, scan speed at 1,000 mm/s, layer thickness at 20 µm, and laser power at 195 watts.

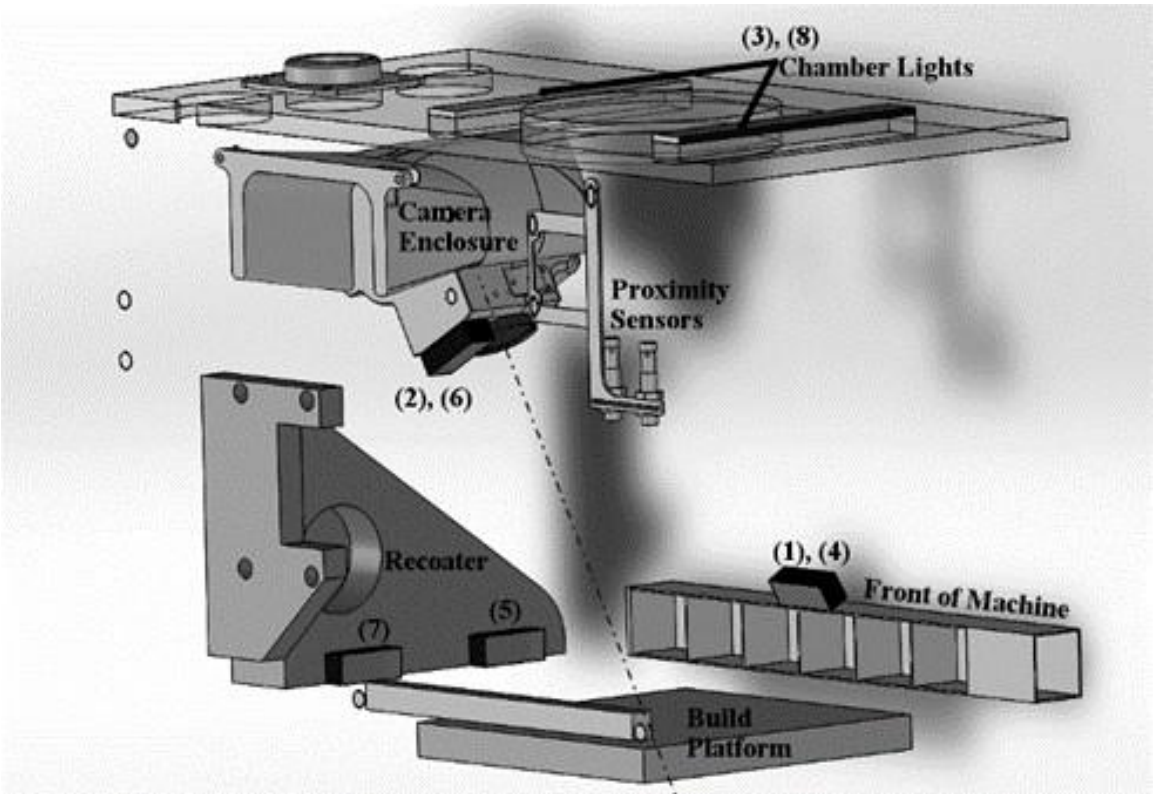

Figure 2.1. Location of camera system and light sources within the build chamber. (1) - (8) sequence and locations of flash modules.

2.3 Test Part Design

A single stainless steel part, denoted as a step cylinder, was built with EOS Stainless Steel GP-1 powder using the EOS standard exposure parameters and processing strategy for 20 µm layers. The 10 mm tall × Ø10 mm cylinder was encircled by a 39-step staircase starting near the base and ending at the top of the part, with a step height of 200 µm (10

layers), displayed in figure 2.2. The small size of the test part was chosen to enable high resolution in the post-build CT scans (i.e. a larger test part would limit the scanning resolution). The 39-step staircase was incorporated into the design to provide unique reference points (i.e. corners of a staircase) to subsequently generate an affine transformation to map labels from CT scan images into camera images, enabling supervised machine learning. Such a mapping is required, given that thermally induced distortions occur during and after the build.

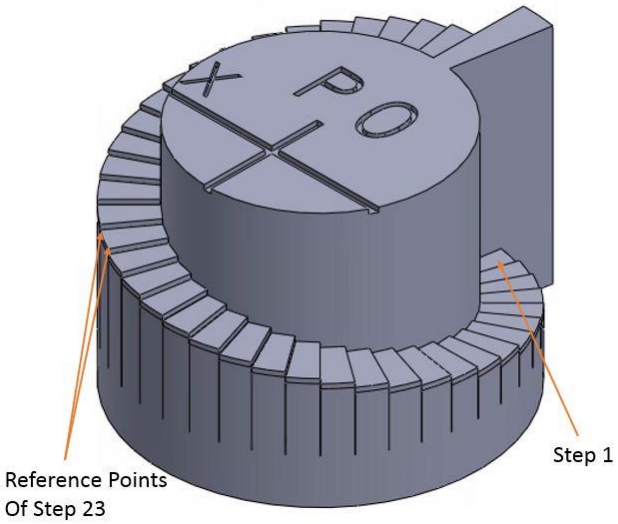

Figure 2.2 3D CAD model of step cylinder. Step 1 and step 23 reference points are shown.

2.4 Data Collection

2.4.1 DSLR Image Data

DSLR camera images of the entire build plate, displayed in figure 2.3, were cropped to a 400 x 400 pixel image centered on the step cylinder and RGB images were down-sampled to produce grayscale representations with intensity values of [0 255]. For each flash module, DSLR images were stacked to create a 3D representation of the build process. Voxels in the DLSR domain were defined based upon image resolution and build

layer height (~50 µm/pixel xy image resolution, 20 µm/layer) in each image stack. The xy resolution provided is an approximation, since the parallax distortion resulting from off-axis imaging leads to varying resolution across the image frame. Then, the intensity I_f is a function of the voxel location x_I, y_I, z_I in the image stack as row, column, and layer as well as the flash module index for each image, $f_I \in \{1, 2, .., 8\}$ in (1).

$$I_f(x_I, y_I, z_I, f_I) \in [0,255] \quad (1)$$

In this investigation the dimensions of the I_f domain, denoted as the DSLR domain, was [400, 400, 555, 8]. Further processing of the DSLR data is detailed later where appropriate. Figure 2.4 displays one layer image for each of the eight flash modules images taken during a single layer of the step cylinder build.

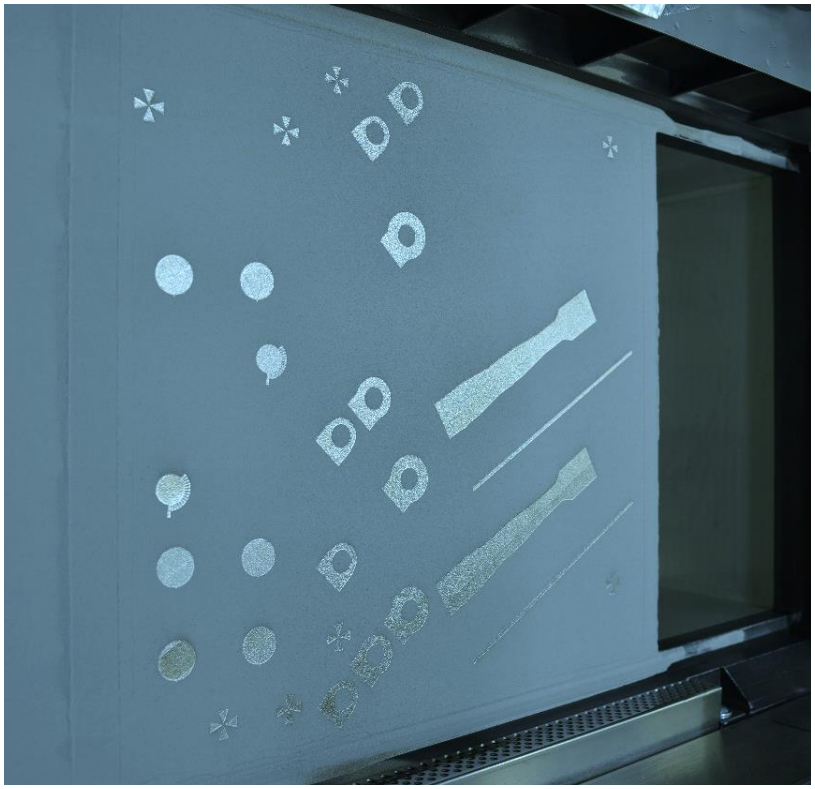

Figure 2.3 DSLR image of the entire build plate from flash module 6.

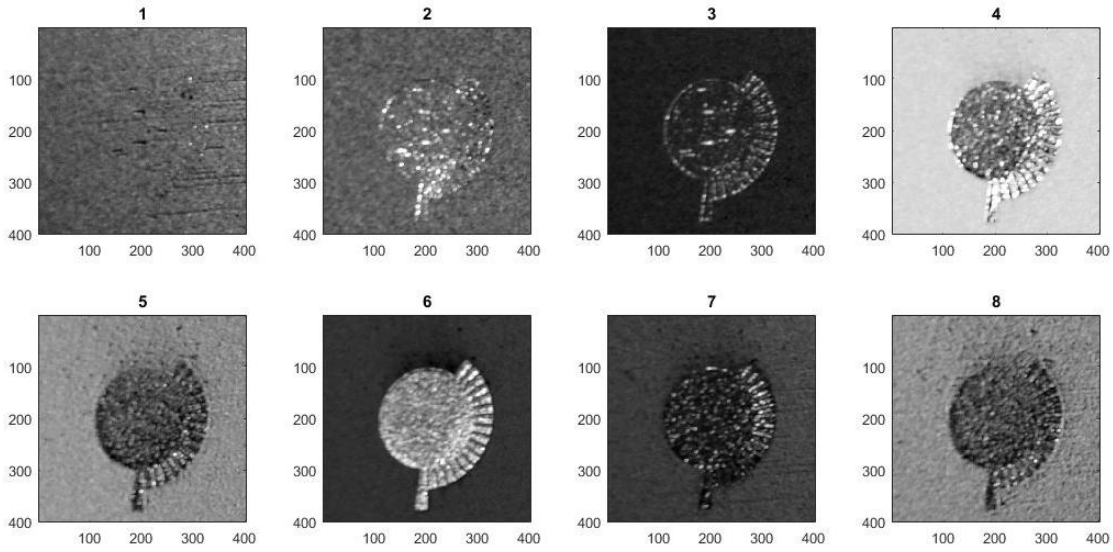

Figure 2.4 Eight flash module images of step 23: (1)-(3) post powder recoating flash modules and (4)-(8) post fusion flash modules.

2.4.2 CT Data

Once the build was complete and the step cylinder was removed from the build plate, post-build CT scans were obtained to create a 3D representation of the part that was subsequently sliced into layerwise images, similar to the DSLR images. Figure 2.5 displays a CT image layer corresponding to step 23. Voxels in the CT images are discretized into 15 µm cubic voxels with intensity values ranging from [0 255]. In the CT domain, gray scale intensity is a function of voxel location (2) where x_{CT}, y_{CT} and z_{CT} represent voxel location for the row, column, and layer.

$$I_{CT}(x_{CT}, y_{CT}, z_{CT}) \in \mathbb{R} \tag{2}$$

The complete CT domain dimensions for the step cylinder was [1009, 1103, 715] in this experiment.

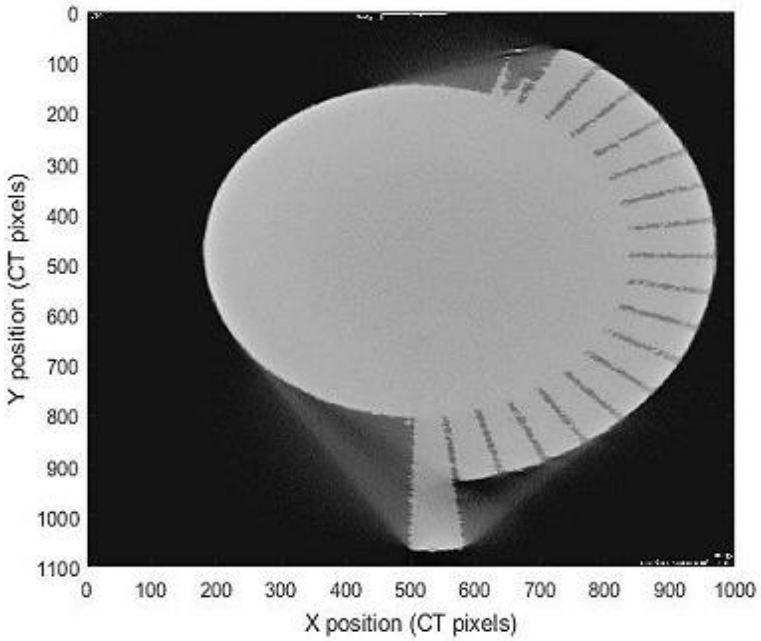

Figure 2.5 CT image layer from step 23

2.4.3 AM System Data

The vectors describing the perimeter of the part in each build layer, hereafter denoted as the SLI domain, were extracted from the EOS M280 system slice files. Slicing data for step 23 are shown in figure 2.6. The SLI domain is to be used as an interim domain for subsequent coordinate transformations. Assuming a well-calibrated laser scanner, no offsets of laser contours and perfect galvanometer calibration the SLI coordinates act as a ground truth, representative of the limits of the EOS M280 laser path.

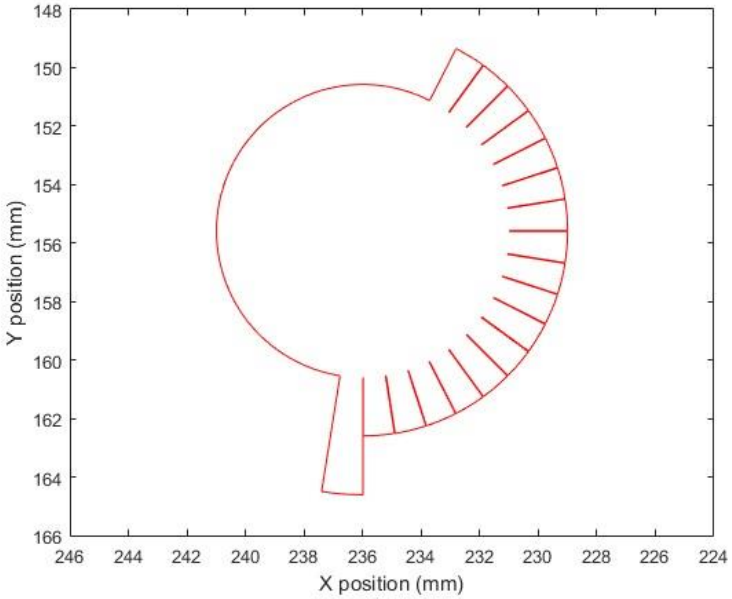

Figure 2.6 Slicing data image of step 23

CHAPTER 3 Ground Truth Labeling

3.1 Identifying Anomalous and Nominal CT Voxels

3.1.1 Defining Anomaly and Nominal CT Voxels

Discontinuities or indications in a part manifest themselves in CT scan images through irregular intensity values as compared to their surroundings, and they are hereafter denoted as anomaly CT voxels. Anomaly CT voxels can be divided into two classes: (i) voids or pores which are low-intensity (low density) CT voxels surrounded by higher intensity (higher density) CT voxels and (ii) super-densities (perhaps as the result of contamination) which are high-intensity (high density) CT voxels surrounded by lower intensity (lower density) CT voxels. Nominal CT voxels, discontinuity and indication free regions of a test part, are observed as CT voxels surrounded by similar intensity CT voxels.

3.1.2 Locating with Convolution Operations

A digital 3D Gabor filter was convolved with the CT image stack to detect the intensity gradients of anomaly CT voxels. CT void or pore voxels will generate large negative convolution responses and super-density CT voxels will generate large positive convolution responses, whereas nominal CT voxels, i.e. smooth regions in the CT images, would generate low valued convolution responses and represent the mean and median of convolution responses. In this investigation the 3D Gabor filter was defined by

$$r_g = \sqrt{{x_g}^2 + {y_g}^2 + {z_g}^2} \tag{3}$$

$$G_{3D}(r, \sigma_g) = \cos(\frac{3}{2}\pi r^2) exp\left(-\left(\frac{r}{\sigma_g}\right)^2\right) \tag{4}$$

Where σ_g is the standard deviation of the underlying Gaussian envelope, r is the distance from the center of the filter and x_g, y_g and $z_g \in Z$ are the coordinates of the kernel in 3D space with values defined by the domain below

$$Z = \left\{ -\frac{(S-1)}{2}, \ldots, +\frac{(S-1)}{2} \right\} \tag{5}$$

The shape of the Gabor filter is defined by the kernel size S in (5), in CT voxels along each Cartesian axis. The use of a symmetric Gabor filter is motivated by the assumption that discontinuities in an AM part can be of any geometry and orientation.

Gabor filter convolution responses from the CT domain were generated with varying kernel sizes, $S = [3,5,7,9,11]$. The selected kernel sizes mimic typical pore and super-density diameters, between 15 µm and 200 µm in diameter, found in metallic PBFAM parts [15]. To simplify analysis, a 3D mask was applied to the domain in order to limit the analysis to the center cylindrical region of the component, thereby excluding the staircase, cylinder edges and build plate background. Figure 3.1 displays a Gabor filter of size S = 11 CT voxels with $\sigma_g = 1$.

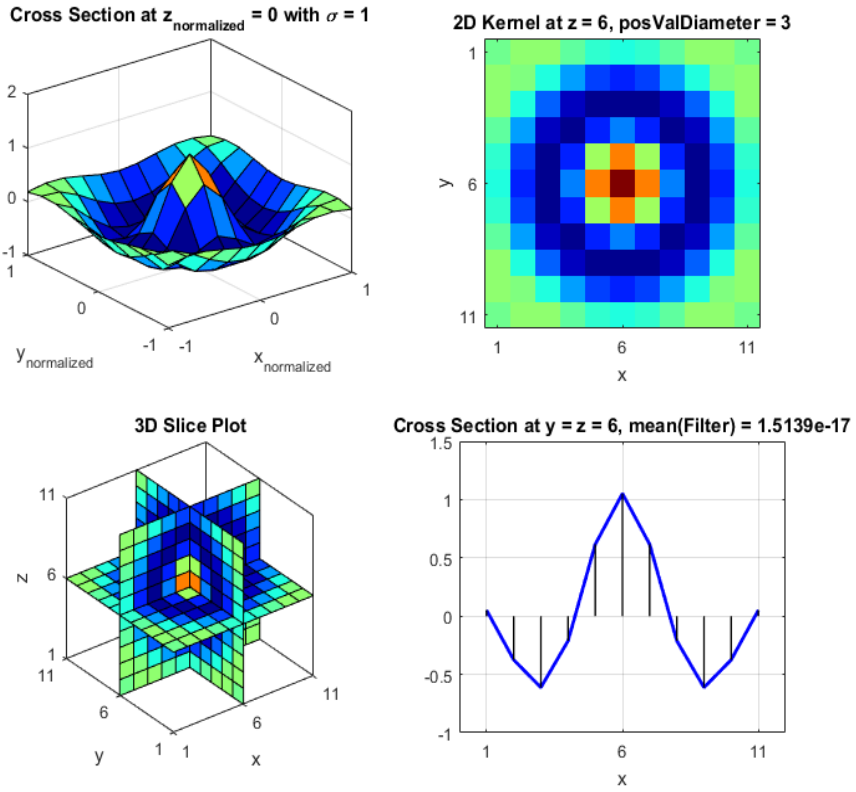

Figure 3.1 Gabor filter with S=11 and σ_g =1.

3.1.3 Locating Anomalous CT Voxels

In this investigation, anomaly CT voxels were identified as having convolution responses falling outside g_a= 5 standard deviations of the mean convolution response of the step cylinder from any set of the responses generated from single Gabor filter sized *S*, where increasing the value of g_a increases the severity and reduces the number of detected anomaly CT voxels. A large standard deviation was chosen to detect the most severe anomalous CT voxels within the large data set of the CT domain. A more severe anomalous CT voxel would potentially be more separable from nominal CT voxels once identified in the DSLR images. A matrix was created to store each set of anomaly CT voxels identified from each Gabor filter size *S* and per anomaly type as anomaly matrices (6) and (7)

$$Ap_r \in \mathbb{R}^{n_p \times 4} \quad (6)$$

$$As_r \in \mathbb{R}^{n_s \times 4} \quad (7)$$

Where Ap_r and As_r represent the pore and super-density matrices respectively, with $r = 1,2 \ldots ,5$ representing a separate matrix for each kernel size *S*, for total of 10 anomaly matrices. $n_p = 3000$ and $n_s = 3000$ where each row in Ap_r and As_r represents a single anomalous CT voxel with stored x, y, z location and convolution response. Additionally, $(n_p + n_s) = 6000$ is approximately equal (i.e. rounded down) to the number of CT voxels whose convolution response fell outside g_a= 5 standard deviations from the mean convolution response, or 0.0000573303% of the CT domain.

3.1.4 Locating Nominal CT Voxels

CT voxels for which the convolution response fell within $g_n = 1$ standard deviation of the mean from the largest Gabor filter size, *S* = 11, were labeled as nominal, where decreasing the value of g_n decreases the number of detected nominal condition CT voxels. Using the largest kernel size ensured located nominal CT voxels were a known minimum distance from any discontinuity containing region (i.e. nominal CT voxels were at least 5 (1/2 of S=11) CT voxels from any anomaly CT voxel). Similar to the construction of A_p, locations (x_{CT}, y_{CT}, z_{CT}) and convolution responses of nominal CT voxels were stored in a matrix N_n with $n_n = 6000$ number of identified nominal voxels chosen randomly from the CT voxels with convolution response within $g_n = 1$ standard deviation of the mean.

$$N_n \in \mathbb{R}^{n_n \times 4} \quad (8)$$

3.2 Labeling and Clustering Anomaly CT Voxels

3.2.1 Clustering Strategy and Implementation for Anomaly CT Voxels

Clustering adjacent anomaly CT voxels into 3D discontinuities, anomaly CT clusters, provides a geometrical description of pores, voids and super-densities that serves as an additional descriptor for ground truth labels. In this investigation, a clustering strategy was generated to identify discontinuities of a specified user-defined minimum size and was implemented with cluster assignment parameters chosen to identify and cluster discontinuities of maximum diameter 200 µm with near minimum diameter of 30 µm.

3.2.2 Initial Screening of Anomaly CT Voxels

Each $r = 1,2 \ldots ,5$ anomaly matrix Ap_r and As_r were combined into two separate anomaly matrixes, one containing all identified pore anomaly CT voxels and another containing all identified super-density anomaly CT voxels. For each of these newly created anomaly matrices, anomaly CT voxels were removed if they lacked $n_{CT} = 3$ neighboring identical type anomaly CT voxels within a radius of $d_v = 2$ CT voxel(s). This removed CT voxel discontinuities which did not have a volume greater than $n_{CT} d_{CT}^3$ = 10,125 µm^3 within a radius of $d_v = 2$ CT voxels of any given Anomaly CT voxel. The remaining anomaly CT voxels were then stored in

$$A_{pt} \in \mathbb{R}^{n_{pt} \times 4} \tag{9}$$

$$A_{st} \in \mathbb{R}^{n_{st} \times 4} \tag{10}$$

The number of anomaly CT voxels was thus reduced to $n_{pt} = 497$ and $n_{st} = 452$ for A_{pt} and A_{st}anomaly matrices, pores and super-density anomaly CT voxels respectively.

With this reduction in the number of anomaly CT voxels, an investigation into the legitimacy of anomaly CT voxels revealed that many of the discovered super-density CT voxels were, in fact, an artifact of CT voxels situated on the edge of the applied mask to the CT domain, where large convolution responses would be present. Conversely, the pore anomaly CT voxels discovered by the initial screening revealed adequate detection of anomaly CT voxels meeting a minimum anomaly CT cluster size. Figure 3.2 shows CT images and convolution response from a detected pore anomaly CT voxel, centered in each image. Note how the intensity value of the pore anomaly CT voxel is different to that of its surroundings, where the kernel response highlights the intensity disparity.

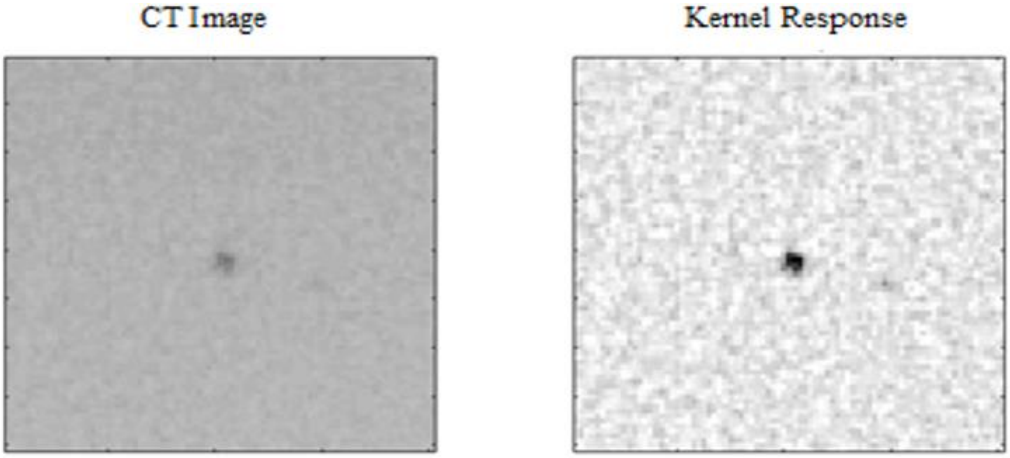

Figure 3.2 CT image (left) and kernel response image (right) of a pore anomaly CT voxel (centered in each image).

The pore anomaly CT voxel irregular intensity values appear quite evident in the CT scan image and convolution response in figure 3. 2. Further analysis of anomaly CT voxels only included the pore CT voxels, the suspected super-density CT voxels were not investigated further.

3.2.3 K-Means Clustering of Anomaly CT Voxels

In order to exclusively assign each pore anomaly CT voxel to an anomaly CT cluster, k-means clustering was performed. Clustering using k-means partitions the anomaly CT voxels into K distinct clusters, minimizing the within-cluster sum of squares of all clusters, i.e. CT voxels in the same cluster are as close to each other as possible and as far away from CT voxels in other clusters [30, 31]. K-means, an unsupervised learning method, was implemented as the number of existing anomaly CT clusters of any size was unknown and assessment of machine learning discontinuity detection *with respect to discontinuity size* was desired.

Conventionally k-means clustering is assessed through silhouette analysis, which displays a measure of how similar a point is to points in its own cluster. However, since the number and size of clusters is unknown and with the potential for many clusters, an alternative metric to identify the number of k_c anomaly CT clusters was generated. The number of k_c anomaly CT clusters was identified by the maximum number of exclusive anomaly CT voxel assignments generated by an imposed cluster number on the set of n_{pt} anomaly CT voxels. Exclusive cluster assignment was defined where an anomaly CT voxel is within k_d voxels of only a single cluster centroid, where $2k_d$ represents the maximum allowable anomaly CT cluster diameter size. Again, typical pore and super-density diameters range between 15 µm and 200 µm in diameter are found in metallic PBFAM parts, therefore $2k_d$ = 200 µm was chosen for the exclusive cluster assignment parameter [15].

The number of exclusive cluster assignments was measured for a range of imposed k-means cluster numbers on the $n_{pt} = 497$ anomaly CT voxels. The number of clusters for k-means was sequentially increased from 1 to k_{maxp} defined in (11) as

$$k_{maxp} = n_{pt}/(n_{CT} + 1) \quad (11)$$

Where $k_{maxp} = 125$ represents the maximum number of possible anomaly CT clusters defined by the minimum requirement for anomaly CT voxels to pass the initial screening detailed previously in 3.2.2. For any imposed k-means cluster number, a low number of exclusive anomaly CT voxel assignments would indicate that either anomaly CT clusters are closely packed (i.e. k-means is possibly over-clustering) or the number of k-means clusters underestimates the true number of anomaly CT clusters. A large number of exclusive anomaly CT voxels assignments would indicate isolated and distinct anomaly CT clusters exist with diameters between 15 µm and 200 µm. The k-means cluster number k_c which generated the largest number of exclusive anomaly CT cluster assignments was chosen as the number of anomaly CT clusters that exist. In this investigation $k_c = 37$ distinct an individual pore anomaly CT clusters were discovered, detailed in figure 3.3 which displays exclusive cluster assignment with respect to number of k-mean clusters imposed on the set of pore anomaly CT voxels.

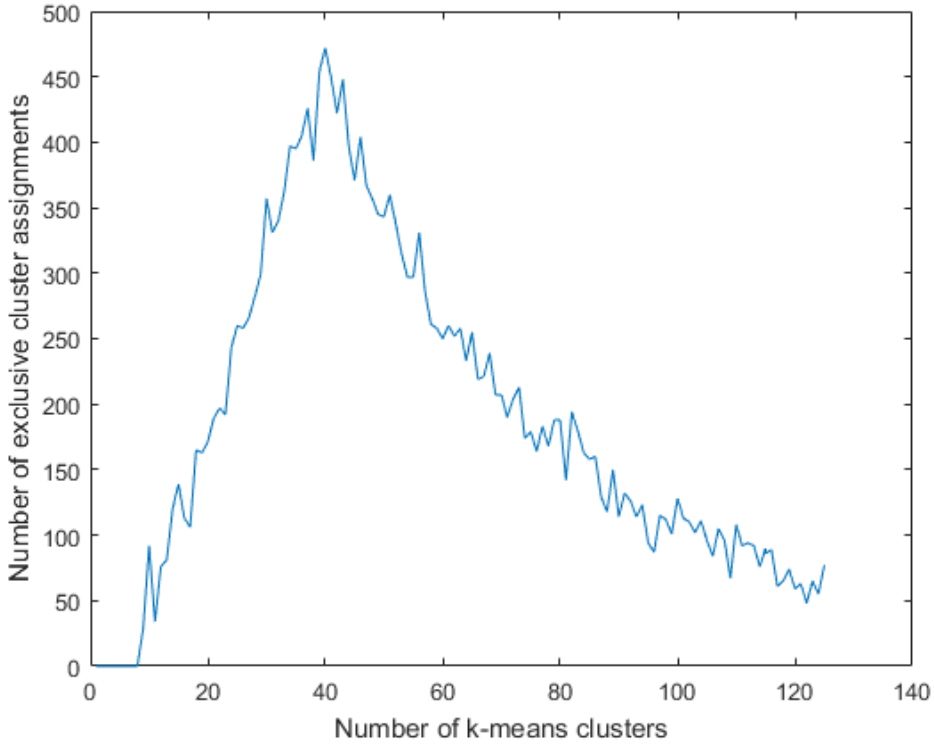

Figure 3.3 Exclusive cluster assignments with respect to number of k-mean clusters for pore anomaly CT voxels.

In figure 3.3 as the number of k-means clusters increases to $k_c = 37$ the exclusive cluster number increases, indicating that the k-means clustering is improving as more clusters are added (i.e. anomaly CT voxels are too far away from the belonging cluster to be exclusive to a cluster). Past $k_c = 37$ the number of exclusive cluster number falls as the increasing number of clusters over fits the true number of anomaly CT clusters.

3.2.4 Further Anomaly CT Cluster Screening

Investigation into the $k_c = 37$ clusters indicated that some anomaly CT clusters were made up of a large anomaly CT cluster overshadowing a smaller anomaly CT cluster, a consequence of using the exclusive cluster assignment metric, as shown in figure 3.4 displaying a single cluster of CT anomaly voxels.

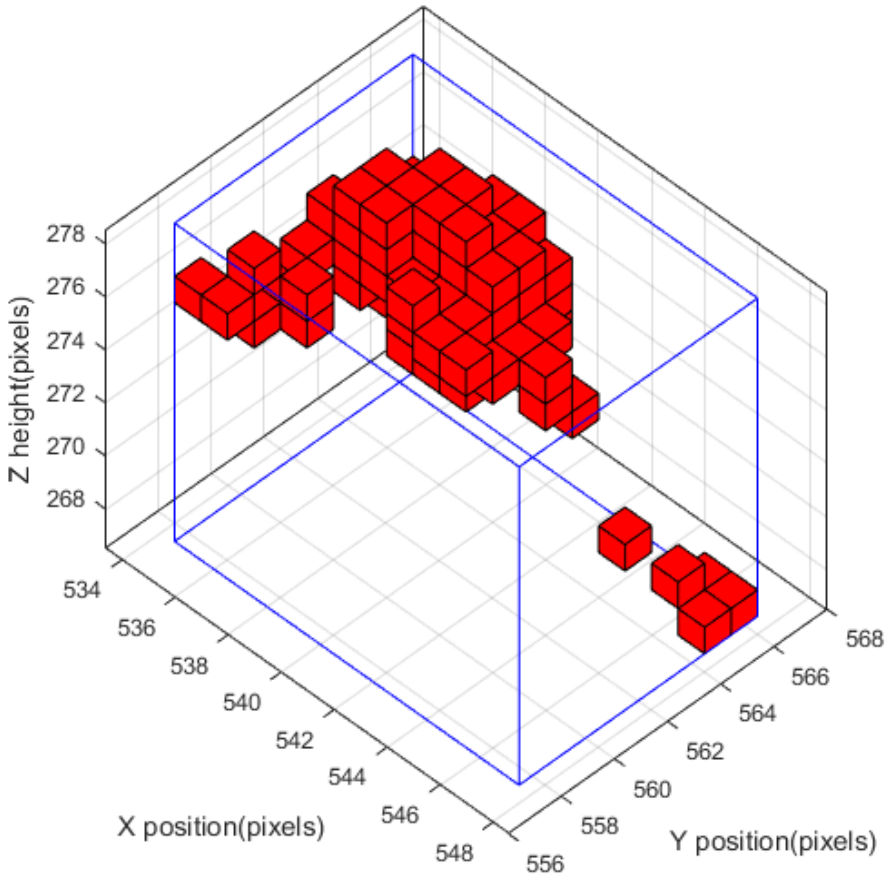

Figure 3.4 An anomaly CT clusters made up of two individual neighborhoods of CT anomaly voxels and outlined occupational volume (in blue) of anomaly CT cluster.

To prevent scenarios as in figure 3.4 a further analysis was used to examined each $k_c = 37$ anomaly CT cluster. For each anomaly CT cluster the packing ratio PR was computed, defined as

$$PR = \frac{T_{CT}}{L_{CT} H_{CT} W_{CT}} \tag{12}$$

Where T_{CT} represents the true volume of an anomaly CT cluster (i.e. number of CT voxels multiplied by the volume of a CT voxel) and L_{CT} , H_{CT}, $and\ W_{CT}$ represent the length, height and width of an anomaly CT cluster, respectively the occupational volume of the cluster, represented as the blue outline in figure 3.4, subsequently the anomaly CT cluster in figure 3.4 has a packing ratio of .064. For each anomaly CT cluster, k-means was again employed to create two clusters (i.e. an anomaly CT cluster

was divided into two anomaly CT clusters) and if the packing ratio of both newly created anomaly CT clusters was greater than that of the original anomaly CT cluster packing ratio then the anomaly CT cluster was split into the two separate anomaly CT clusters. This methodology of screening only accounts for cases where a large anomaly CT cluster overshadows a smaller anomaly CT cluster and where k-means, combined with exclusive cluster assignment metric, lacks the discriminatory power to individually cluster the two anomaly CT clusters separately. However, this methodology only assumes that an anomaly CT cluster can only be further split into two anomaly CT clusters. In scenarios where further deconstruction of an anomaly CT cluster could take place (i.e. a large anomaly CT cluster overshadows two or more smaller clusters) the entire local region would be assumed to be a single phenomenon to be studied and therefore be labeled just as a single anomaly CT cluster.

In this investigation three of the original $k_c = 37$ anomaly CT clusters were split into six anomaly CT clusters, using the packing ratio and k-means analysis, yielding a total of 40 pore anomaly CT clusters made up of the $n_{pt} = 497$ anomaly CT voxels. Figure 3.5 depicts the anomaly CT clusters from figure 3.4 split, where the packing ratio improved from 0.064 on the single cluster to 0.312 and 0.199 on the partitioned clusters. Figure 3.6 depicts an anomaly CT cluster that was not split using this method.

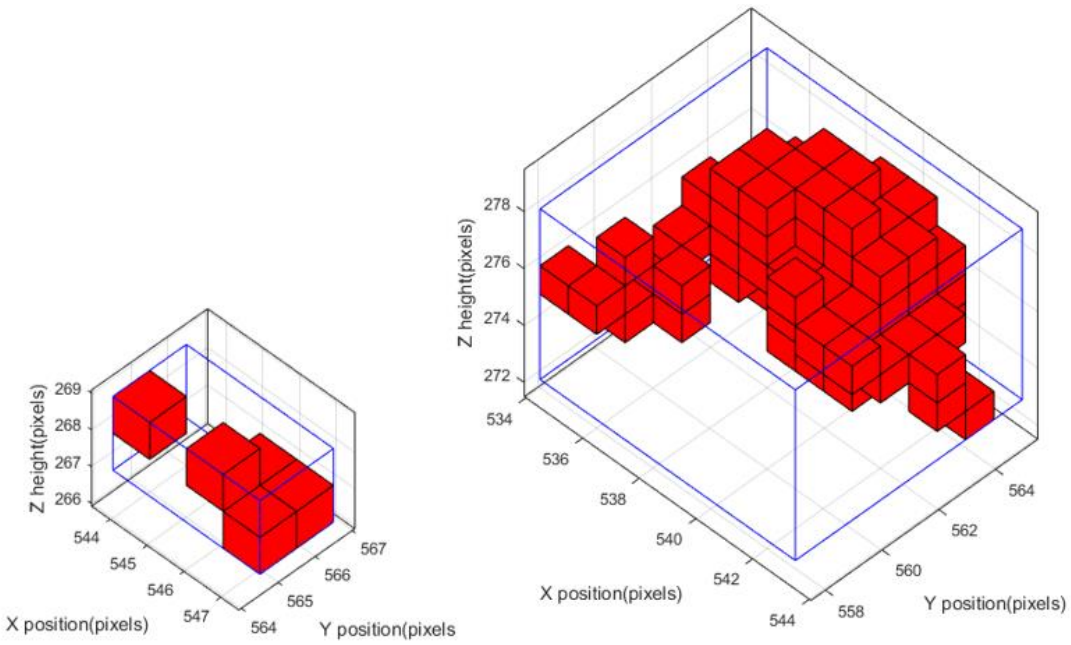

Figure 3.5 The anomaly CT cluster shown in figure 3.4 is split into two individual CT clusters whose packing ratio is now 0.312 and 0.199 respectively.

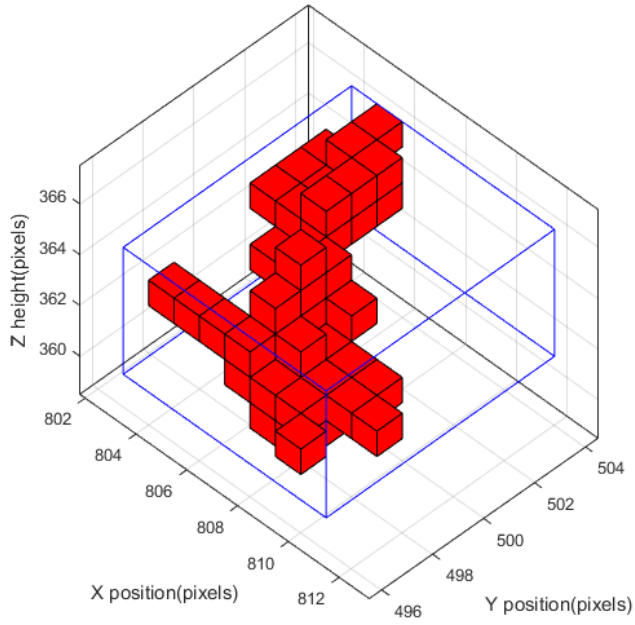

Figure 3.6 An anomaly CT cluster which was not split.

3.3 Examination of Ground Truth Labels

3.3.1 Anomaly and Nominal CT Voxels

Figure 3.7 displays a nominal and anomaly CT voxel in both a CT image slice (80x80 CT pixels) and a kernel response of both in another image slice (80x80 CT pixels), images are colored-scaled identically. The smoothness in the CT image and kernel response for the nominal CT voxel highlights the discontinuity that exist in the anomaly CT voxel.

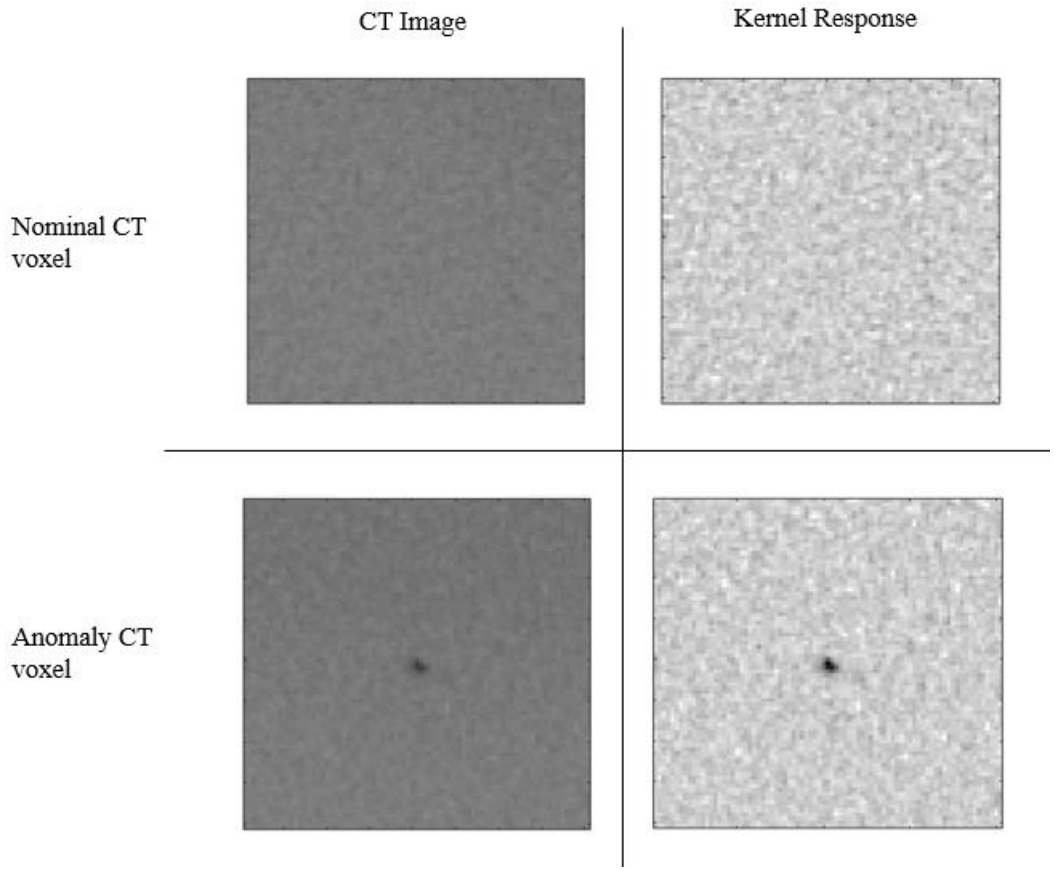

Figure 3.7 Anomaly and nominal CT voxel in CT image (left) and S = 11 Gabor filter Response (right).

3.3.2 Anomaly CT Clusters

Using the location of discovered anomaly CT voxels paired with cluster assignments, the CT scan data can be viewed in a layerwise manner to depict the

geometry of an anomaly CT cluster as seen in the CT images; figure 3.8 shows an anomaly CT cluster as seen in the CT scan images, represented earlier in figure 3.6 above. Each layer in figure 3.8 is centered on the anomaly CT cluster centroid location, with image dimensions set to 80x80 CT pixels (1200x1200 microns). Layers 360-364 were identified to contain an anomaly CT voxel, while layers 359 and 366 did not.

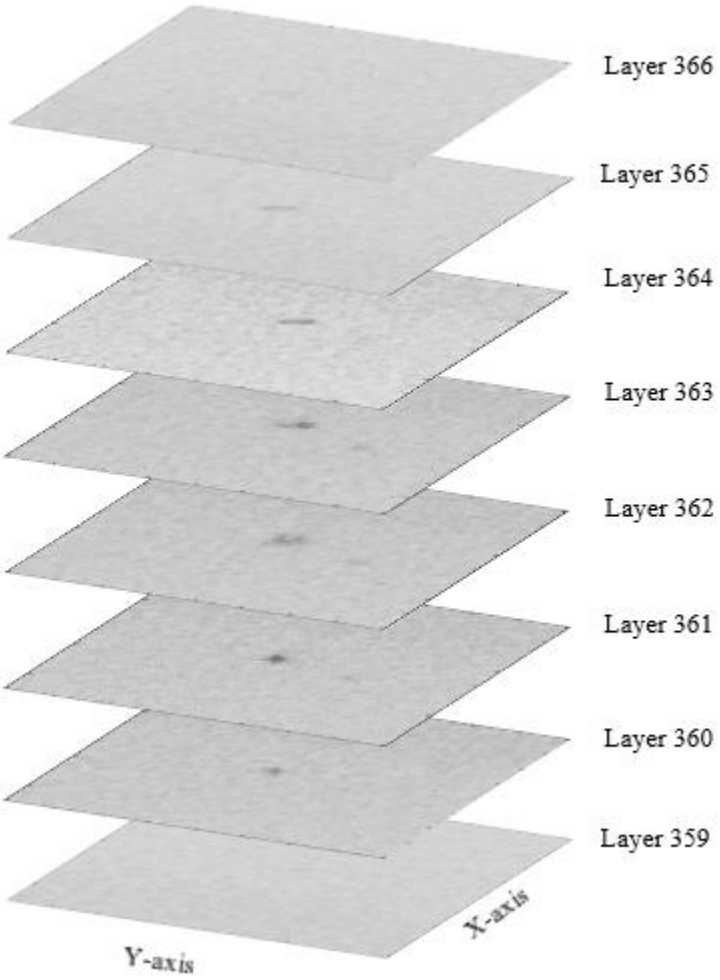

Figure 3.8 CT scan view of an anomaly CT

The anomaly CT voxels shown in figure 3.8 illustrate that during the build the position of the anomaly is not uniform (i.e. cross-sections of the anomaly cluster shift between layers). This reason for this shift is not currently well understood.

Anomaly CT clusters were divided into five classes based on the number of CT voxels in each cluster [4-7, 8-11, 12-15, 16-19, >20], corresponding to the volume of each cluster, [13.5-23.6, 27.-37.1, 40.5-50.6, 54.0-64.1,>67.5 x 10^3 μm^3], and the diameter of a spherical discontinuity that would have equivalent volume [29.5-35.6,37.2-41.4,42.6-45.9,46.9-49.7, >50.5 µm]. The frequency of each cluster size class and the total number of voxels per class in the CT domain are displayed in figure 3.9 in blue and green, respectively.

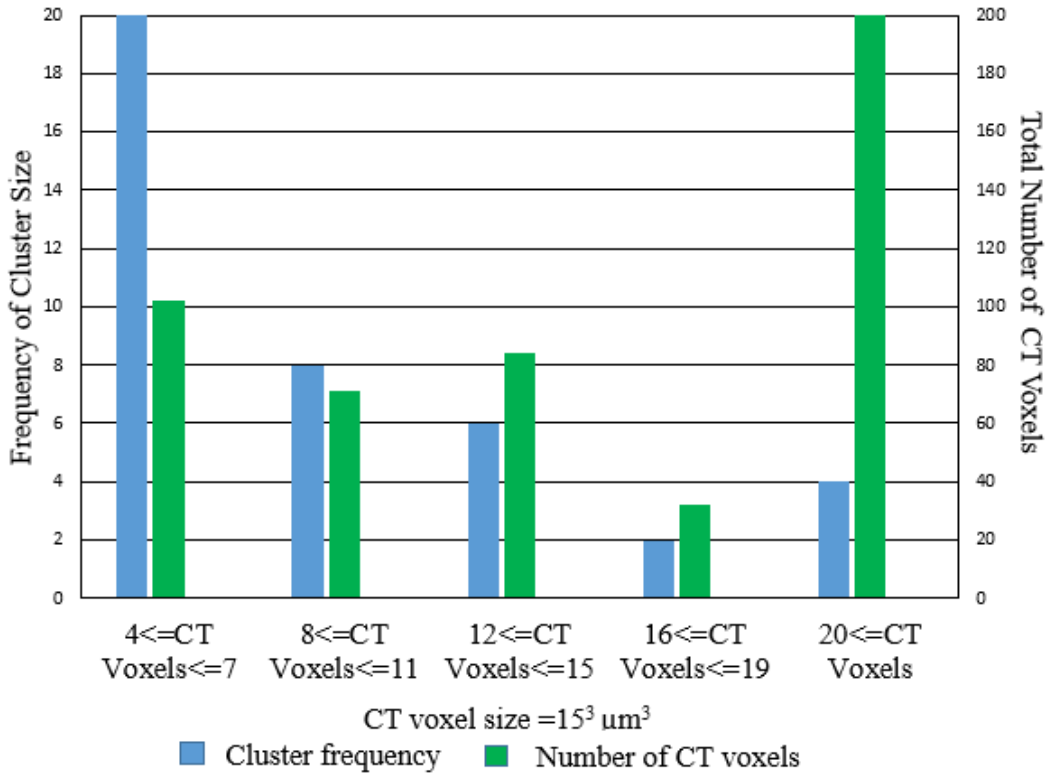

Figure 3.9 Frequency of CT cluster class size (blue – left axis) and total number of CT voxels per class (green – right axis).

Figure 3. 9 indicates there are many smaller anomaly CT clusters, however most anomaly CT voxels belong to larger anomaly CT clusters. The location of all anomaly CT clusters with respect to the step cylinder part outline is depicted in figure 3.10. The distribution of anomaly CT clusters reveals that a large number of anomaly CT clusters

are located near the center of the part, however it is worth noting that the mask applied to the CT domain limited the discovery of anomaly CT voxels to the center cylindrical region. CT clusters in figure 3.10 are color coded to the match the cluster sizes depicted in figure 3.9, where magenta, red, green, blue, and cyan represent [4-7, 8-11, 12-15, 16-19, >20] cluster categories respectively. Anomaly CT clusters depicted in figure 3.9 with multiple colors in one region indicate neighboring clusters.

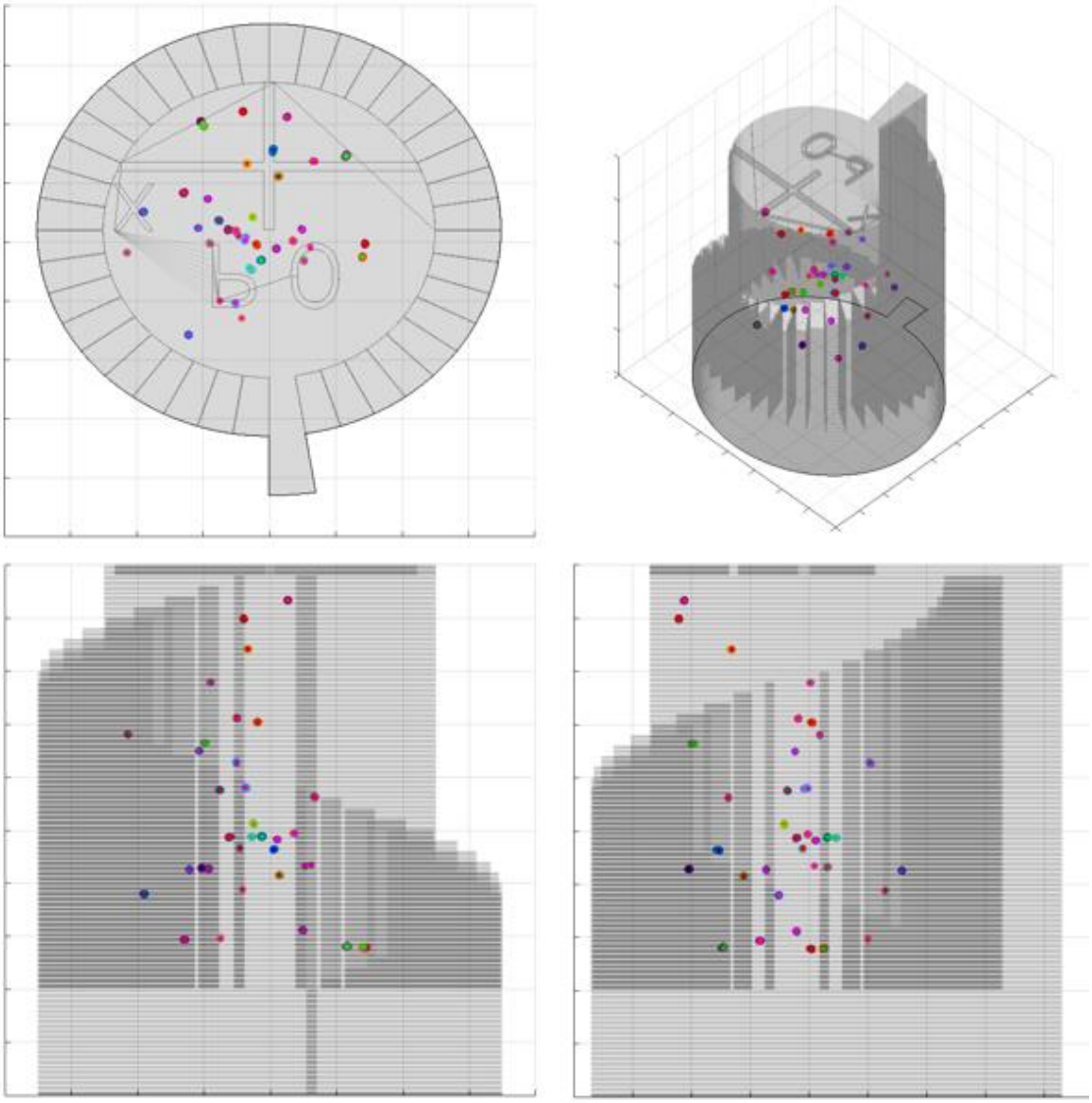

Figure 3.10 Location of all discovered anomaly CT clusters in the SLI domain within the transparent cylinder shown in front, side, top and isometric view.

CHAPTER 4 DSLR Domain Ground Truth Labeling and Feature Extraction

4.1 Ground Truth Labeling the DSLR Domain from the CT Domain

4.1.1 Need for Coordinate Transformation

Locations of anomaly and nominal CT voxels, *x*,*y*,*z* coordinates of the CT voxels in the CT domain, were mapped into the DSLR domain to label *x*,*y*,*z* coordinates of DSLR voxels in the DSLR domain. An affine coordinate transformation was generated by using the corresponding *x*,*y*,*z* locations of the staircase corners in the CT and DSLR domains.

4.1.2 Extracting Reference Points

The two corners on the top of each step in the staircase, a total of 78 coordinates, acted as reference points to build the affine coordinate transformation and were manually labeled. Each flash module image stack was treated as having a separate coordinate system, accounting for a vertical (z-axis) translation of the build plate during the powder recoating process causing slight offsets, in the x and y direction, denoted as flash shift. The flash shift is the result of capturing images while the z-axis translation of the build plate was taking place. The SLI domain was used as an interim domain between CT and the eight DSLR flash module image stacks, therefore ten sets of coordinates were extracted from these domains. The SLI domain acted as a ground truth for the laser path, and was used to improve the coordinate transformation due to noisy extraction of reference points in the CT and DSLR domains.

4.1.3 Coordinate Transformation

Coordinate transformations were generated between domains using a linear least squares approach for matching a set of reference points, provided by the staircase,

which produced a corresponding affine transformation, i.e. rotation and translation. The order of constructed coordinate transformations was: CT to SLI, DSLR flash modules to SLI, and fusion of CT to SLI and DSLR flash modules to SLI, thereby creating eight CT to DSLR flash-module coordinate transformations.

In this investigation, only the coordinate transformation of the CT domain to first flash module of the DSLR domain was implemented followed by application of translation vectors to the place ground truth labels in the remaining 7 DSLR flash module image stacks. Translations were equal to the difference in the translation vectors between CT domain to DSLR flash module image stack 1 and CT domain to the remaining DSLR flash image stacks. Use of only one CT to DSLR transformation was enacted to prevent a difference in the down-sampling of data between CT to DSLR image stacks due to non-exact solution arising from the constructed coordinate transformations and difference in voxel discretization. The difference in the discretization between CT domain and DSLR domain meant multiple anomaly CT voxel coordinates would be mapped to the same DSLR voxel location. Figure 4.1 depicts the difference in size between CT and DSLR voxels which causes the down-sampling between CT and DSLR domains.

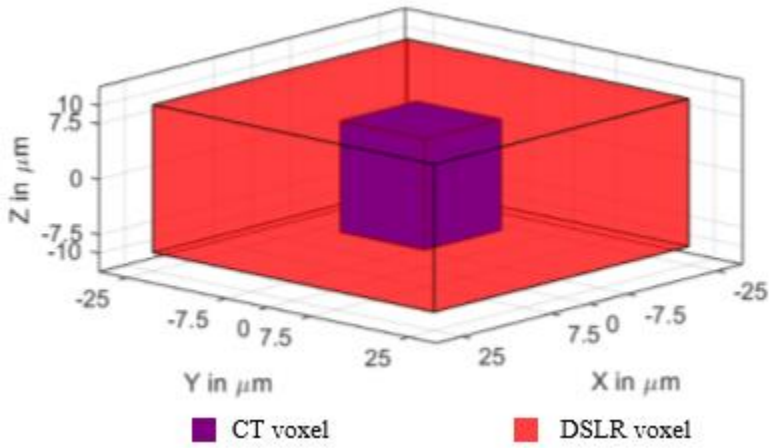

Figure 4.1 CT voxel compared to DSLR voxel.

The DSLR transformation between the CT domain and DSLR flash module 1 image stack was generated and figure 4.2 displays locations of transformed reference points from the CT domain and locations of observed reference points in the DSLR flash module 1 image stack.

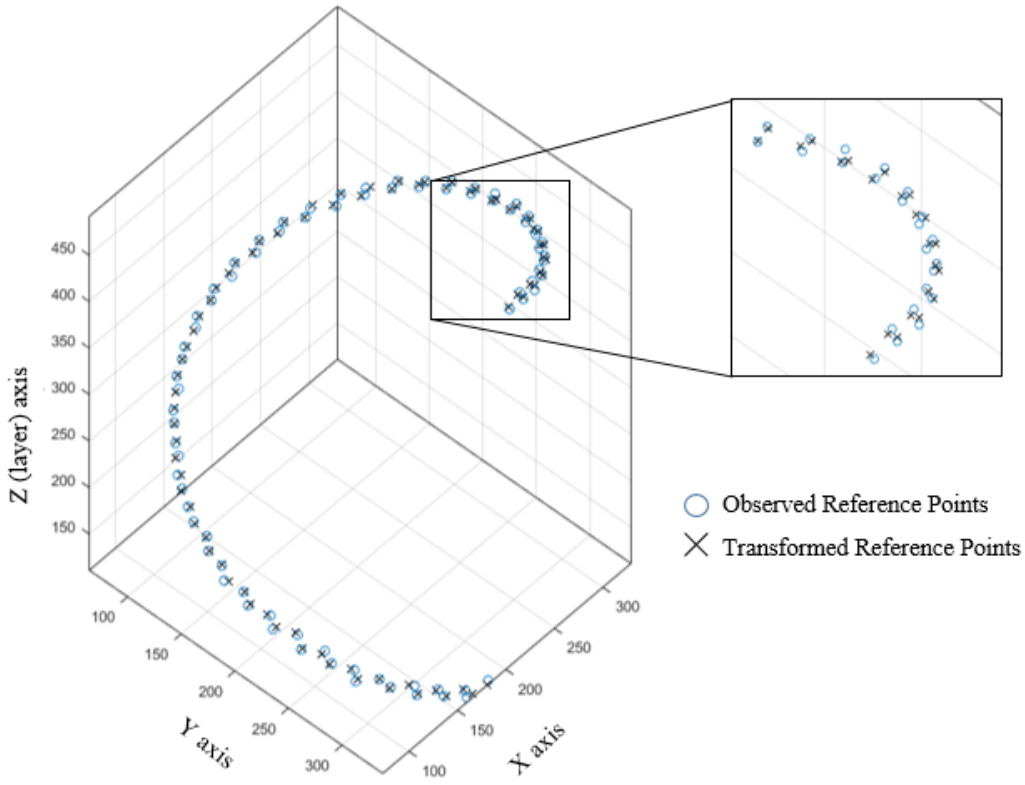

Figure 4.2 Observed and transformed reference points in flash module 1 domain.

The error of the coordinate transformation was calculated to assess the accuracy of the transformation (and possible impact of the distortion); error was defined as the displacement between observed and transformed reference points in the DSLR image stacks and was calculated separately for the x, y and z coordinate axis. Figure 4.3 is a histogram displaying the calculated error between the observed and transformed reference points, displayed in figure 4.2, in each Cartesian axis of flash module 1 image stack. Error in the z direction was minimized, as step height was fixed and correlated well with build layer images, while the largest error was in the x and y directions, where voxel discretization interfered with the hand labeling.

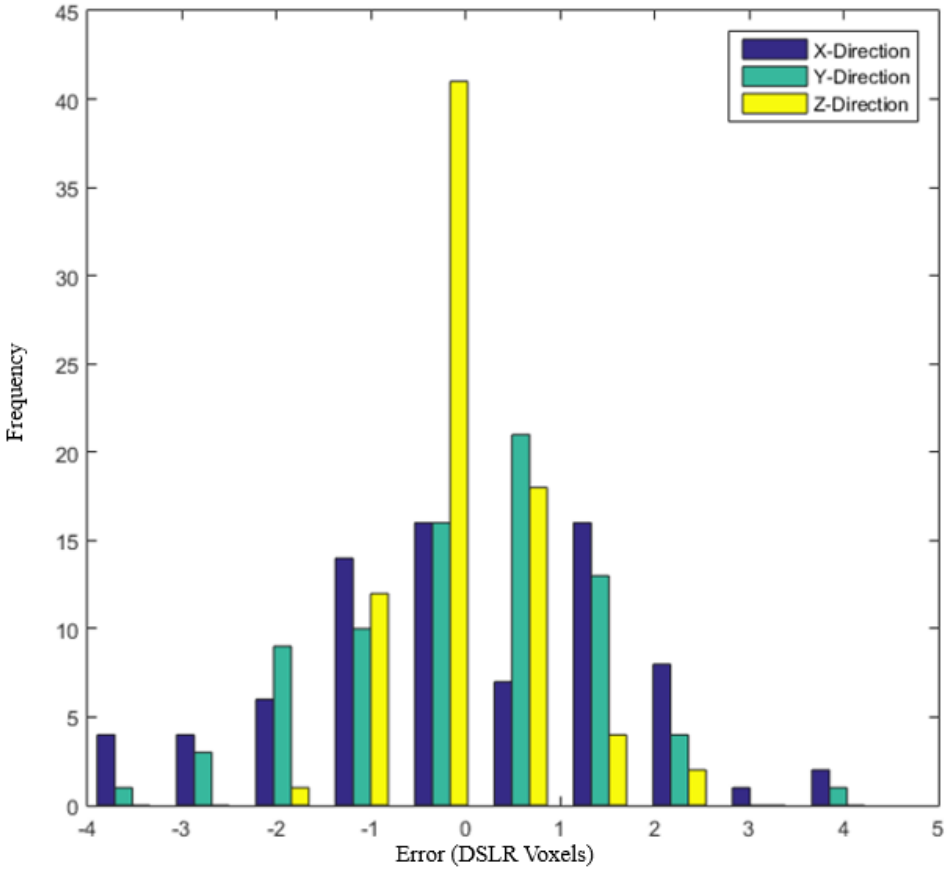

Figure 4.3 Histogram of reference point coordinate transformation error in the DSLR flash module 1 domain for the x, y and z axis.

Flash shifts, the difference in translation vectors between the CT to DSLR flash module 1 image stack coordinate transformation and the remaining CT to DSLR flash module image stack coordinate transformations, are displayed in table 4.1 in terms of DSLR voxels.

Table 4.1 Flash Shift of DSLR modules with respect to DSLR flash module 1.

Flash module number	X coordinate shift (DSLR voxels)	Y coordinate shift (DSLR voxels)
2	0	0
3	-2	-1
4	-1	-2
5	-1	-2
6	-1	-2
7	0	-1
8	3	-2

Using the coordinate transformation and subsequent flash shift translations, 180 DSLR anomaly voxels locations were labeled as anomalous from the 497 anomaly CT voxel locations transformed into each DSLR flash module image stack. The number of nominal DSLR nominal voxels was reduced and rounded down to 1600 DSLR voxels labeled corresponding to the 6000 nominal CT voxel locations identified and transformed in the DSLR flash module image stacks. Cluster labels for each anomaly CT voxel remained intact during coordinate transformation into the DSLR flash module image stacks. Cluster size definition was shifted to [1, 2, 3, 4, >5] DSLR voxels, altered from the CT voxel categories displayed figure 3.8, where figure 4.4 displays the frequency (in blue) and total number of belong anomaly DSLR voxels (in green) for each anomaly DSLR cluster.

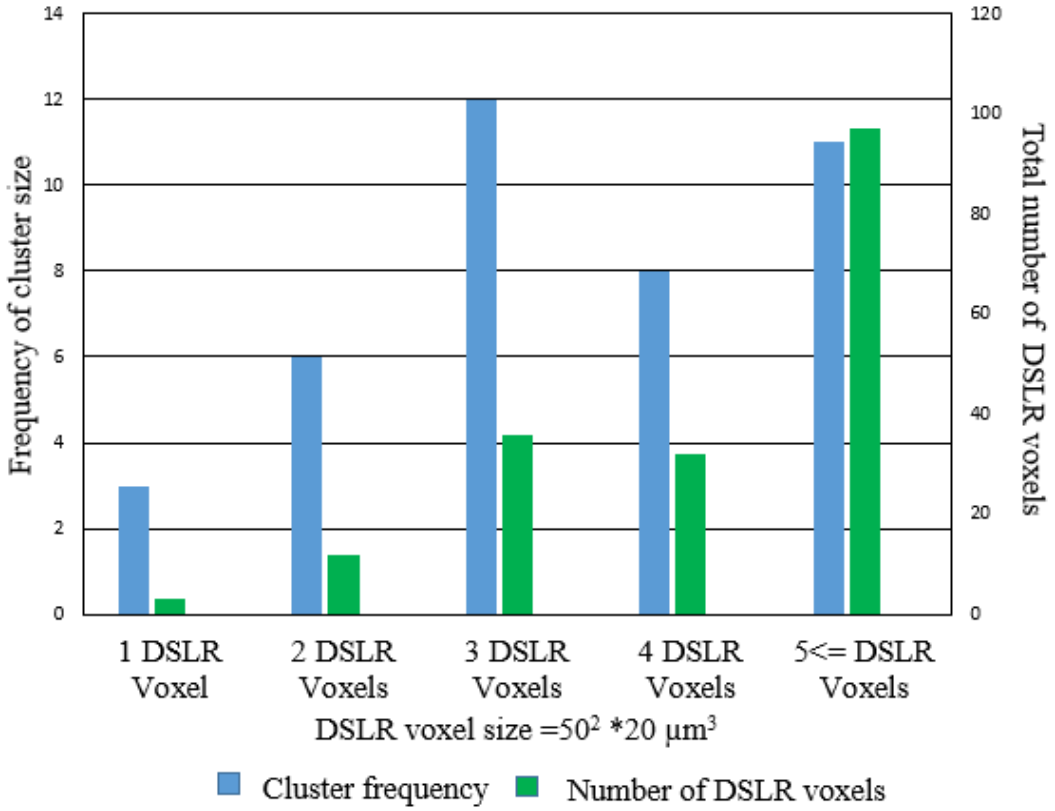

Figure 4.4 Frequency of DSLR cluster size class (blue – left axis) and total number of DSLR voxels (green – right axis) per class.

Figure 4.4 displays that now a majority of anomaly DSLR voxels are in larger anomaly DSLR clusters. Table 4.2 displays the distance to anomaly DSLR cluster centroids for all anomaly DSLR voxels.

Table 4.2 Displacement (DSLR voxels) to anomaly cluster centroid for anomaly DSLR voxels.

DSLR Voxel displacement to Anomaly Cluster Centroid	Z Axis	X Axis	Y Axis
-2	5	n/a	3
-1	37	30	41
0	115	126	106
1	20	30	28
2	3	1	2

Table 4.2 reveals that the labeled anomaly DSLR voxels fall within one voxel of its cluster centroid; distance to anomaly centroids in the DSLR domain were defined

in Cartesian axis coordinates due to the difference is discretization of the DSLR domain. Figure 4.5 displays the coordinate transformation performed on a region of the step cylinder, transformed from the CT domain into flash module 3 image stack of the DSLR domain.

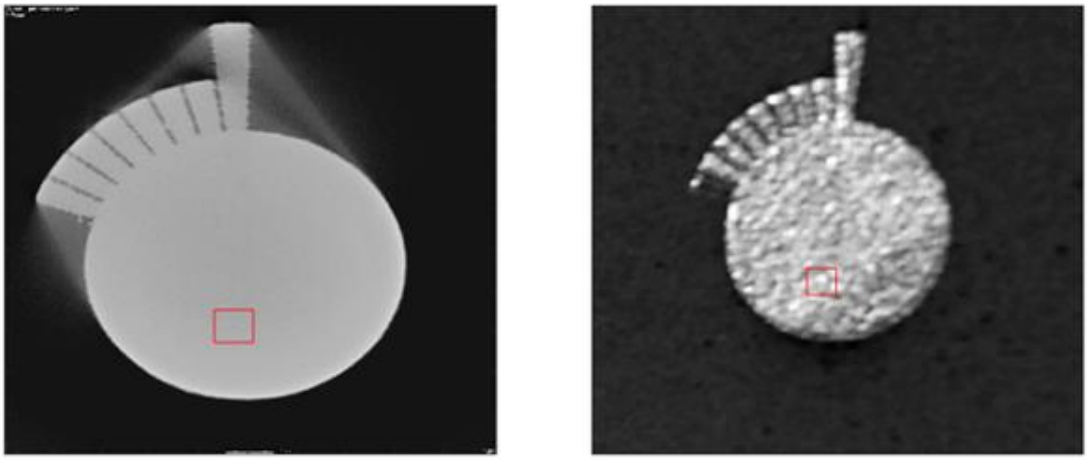

Figure 4.5 Coordinate transformation of red outlined region from the CT domain (pictured left) into flash module 3 image stack (pictured right).

4.2 Feature Extraction from DSLR Flash Module Image Stacks

4.2.1 Linking Coordinate Transformation to Feature Extraction

Residual errors in the generated coordinate transformation can arise due to the non-exact extraction of reference points caused by inaccurate labeling, distortion of the component in a nonlinear, non-affine manner during the build, or by a non-exact solution for a linear least square generated coordinate transformation. If an error in the coordinate transformation is present and ground truth labels are located incorrectly in the DSLR domain without accountability or certainty, then feature extraction from the DSLR domain would potentially include mislabeled features and discontinuity detection would not be successful. Generating a metric for evaluating the performance of the generated coordinate transformation can be used to formally define a feature

extraction filter, e.g. the size, to ensure accurate extraction of a transformed CT ground truth label from the DSLR domain. A larger feature extraction filter, centered on a transformed coordinate into the DSLR domain, can help to ensure accurate extraction of a transformed ground truth label from the DSLR domain for latter machine learning classification, but would involve extraction of more data. Defining a feature extraction filter which maximizes accuracy that information pertaining a transferred label is extracted while minimizing the size of the filter is crucial.

In this investigation, the size of the feature extraction filter to be used was defined by the root mean square error (RMSE) in each Cartesian axis of the employed coordinate transformation, represented in figure 4.3. RMSE in each Cartesian axis can be defined as

$$\mathrm{RMSE}_x = \sqrt{\frac{\sum_{\mathrm{j}=1}^{\mathrm{n}_r}\left(\mathrm{x}_j - \hat{x}_j\right)^2}{\mathrm{n}_r}} \tag{13}$$

$$\mathrm{RMSE}_y = \sqrt{\frac{\sum_{\mathrm{j}=1}^{\mathrm{n}_r}\left(y_j - \hat{y}_j\right)^2}{\mathrm{n}_r}} \tag{14}$$

$$\mathrm{RMSE}_z = \sqrt{\frac{\sum_{\mathrm{j}=1}^{\mathrm{n}_r}\left(\mathrm{z}_j - \hat{z}_j\right)^2}{\mathrm{n}_r}} \tag{15}$$

Where $(x_j,\ y_j,\ z_j)$ represent the $n_r = 78$ observed DSLR domain reference points and $(\hat{x}_j,\ \hat{y}_j,\ \hat{z}_j)$ represent the $n_r = 78$ transformed DSLR domain reference points. In this investigation RMSE of the reference points was calculated using equations (12), (13), and (14) in all DSLR domain image stacks, where the maximum RSME across all DSLR domain image stacks was ~1.75, ~1.5, and ~0.75 DSLR voxels in the *x,y,z* directions corresponding to 87.5, 75, and 37.5 µm respectively. The RMSE

of the reference points in flash module 1 image stack, depicted in figure 4.3, was 1.65, 1.5, 0.75 DSLR pixels in the *x,y,z* directions respectively .

4.2.2 Defining Feature Extraction Filter Size

Defining the size of each Cartesian axis of a feature extraction filter in terms of coordinate transformation RMSE builds confidence in the ability to perform proper and useful data extraction. In this investigation, a 3-dimensional filter was used for feature extraction, whereby the surrounding neighborhood of the ground truth label contributes to the DSLR feature description for machine learning classification. Based on the understanding of the physical processes that occur, it was deemed critical to assess features from multiple layers and the surrounding local region in order to accurately identify discontinuities or indications in the final component; the fusion zone from laser melting may extend several layers during the laser exposure operation and indications of a discontinuity can potentially be in previous (or subsequent) build layers.

A feature extraction filter with size of (x_f, y_f, z_f), respectively the length, width and height of the filter, can be defined in terms of coordinate transformation RMSE as

$$x_f = RMSE_x \; 2 \; L_s \tag{16}$$

$$y_f = \mathrm{RMSE}_y \; 2 \; L_s \tag{17}$$

$$z_f = \mathrm{RMSE}_z \; 2 \; L_s \tag{18}$$

Where L_s denotes the number of standard deviations to be used. Defining filter size in terms of coordinate transformation RMSE guarantees a predefined level of confidence when transferring labels from the CT to the DSLR domain. In this investigation $L_s = 2$, meaning that the feature extraction filter, centered on a labeled CT coordinate and then transferred into the *in situ* sensor domain, captured and

extracted the information pertaining to the properly labeled and transformed CT to DSLR coordinate with 95% confidence (corresponding to ±2 standard deviations). Increasing L_s increases the confidence that the transferred label is within the feature extraction filter; however it also increases the number of features and thereby increases the dimensionality of the feature space used for machine learning.

To maintain consistency of feature extraction across all DSLR flash module image stacks, the largest RMSE in the *x,y,z* direction from the eight CT to DSLR flash module image stacks was used across the entire DSLR domain, found to be ~1.75, ~1.5, and ~0.75 DSLR voxels in the x, y, and z directions. Using the maximum RMSE ensured that the confidence of capturing the information associated with labeled DSLR voxel was at least 95% in all flash module image stacks.

Using the filter size definitions in (16) - (18) the feature extraction filter size was 7 x 6 x 3 DSLR voxels, however the filter was expanded to 7 x 7 x 3 DSLR voxels so as to be square in the xy-plane. Figure 4.6 depicts an outline of the feature extraction filter in a post-fusion and post powder recoating flash module image stack for a labeled anomaly DSLR voxel. Each DSLR flash module layer image is 25 x 25 DSLR voxels (1250 x 1250 µm) and the red outline indicates the filter, 7 x 7 x 3 DSLR voxels (350 x 350 x 60 µm), which is centered on the labeled DSLR voxel.

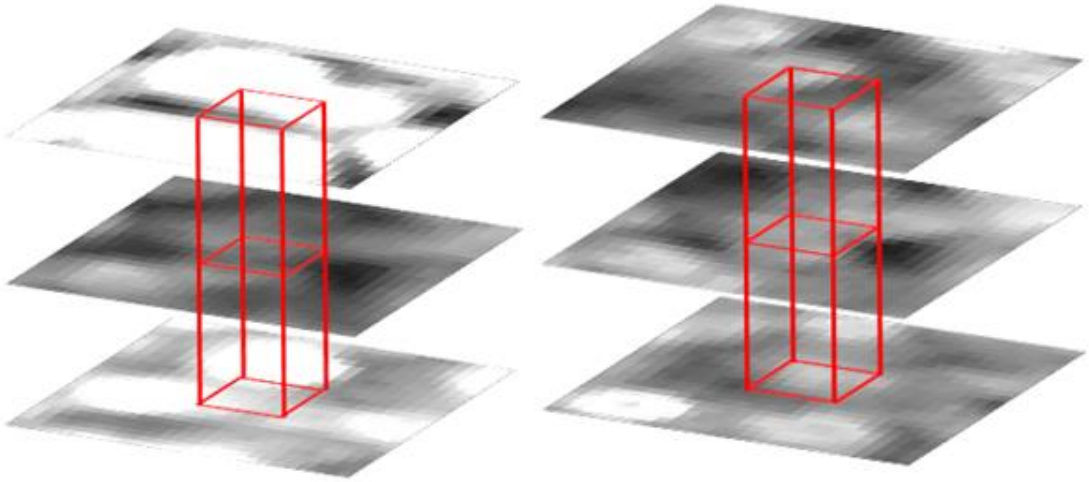

Figure 4.6 Outline of feature extraction filter over a ground truth anomaly in two DSLR flash module domains.

4.2.3 Feature Extraction

Given any filter size (x_f, y_f, z_f), $F_n = x_f y_f z_f$ linearly-independent filters for feature extraction can be created, where one filter extracts one feature. This is done by setting only one filter element to 1 at a time, while the remaining $F_n - 1$ elements in a filter are set to zero and then performing a convolution operation between the filter and location of the ground truth label in the DSLR flash module image stack. In this manner any additional filter constructed would be a linear combination of the first F_n filters and thus contain no additional information for latter linear machine learning classification.

In this investigation $F_n = 7\ x\ 7\ x3 = 147$ where each filter extracts an intensity value from a DSLR voxel as one feature dimension, the entire set of filters extract the neighborhood of DSLR voxel grayscale intensities surrounding and including the ground truth label in the DSLR domains. The same sized feature extraction filter was used in each of the 8 individual DSLR flash module domains,

therefore $8F_n = 1176$ feature descriptions were extracted (from all 8 DSLR domains) for each ground truth label assigned to an *x,y,z* location.

In this investigation, a feature matrix M_f was generated for each set of anomaly and nominal features extracted from each DSLR flash module image stack where

$$M_f \in \mathbb{R}^{n_{total} \times F_n} \qquad f = 1,2,..,V \tag{19}$$

where n_{total} represents the total number of data samples (i.e. individual *x,y,z* locations within the DSLR domain), both anomalous and nominal, and $F_n = 147$ represents the total number of extracted features. A feature matrix M_f is generated for every individual DSLR flash module image stack $f = 1,2,..,V$ whereby $V = 8$. $\vec{x}_{fi}$ represents a feature vector for each f feature matrix and sample $i = 1,2,\dots,n_{total}$ with class label $y_i \in \{-1,+1\}$, where -1 represents nominal and +1 represents anomaly. Each feature dimension of each feature matrix was then set to zero mean and unit standard deviation for all samples.

4.2.4 Sample Size for Discontinuity Detection

In an ideal supervised learning-based classification scheme a one-to-one ratio of binary labels would be used for training, where the number of training samples would be greater than the number of features. However, AM system process parameters and ground truth anomaly detection can limit the number of anomalous samples present, i.e. optimized processing conditions are expected to generate minimal indications and discontinuities to study. This can lead to a scenario where the number of total samples (i.e. number of anomaly and nominal DSLR voxels) is less than the number of features if a one-to-one ratio is used, possibly negatively affecting the machine learning model training process. Attempting to generate an increase in

anomalous part behavior, e.g. by altering processing conditions, would potentially limit the number of nominal samples. Therefore, a one-to-one ratio of nominal to anomalous samples might not be possible in any reasonable build that is representative of a real application when using binary labels. There is no formal mathematical calculation to define how large sample size must be compared to the dimension of the feature space. However, accurate classification of testing data with similar classification models in a cross-validation scheme can be used to validate results and determine if sufficient sample size was used [32].

The down-sampling during mapping between CT and DSLR domain reduced the number of anomalous samples available for labeling and training. With 180 anomalous DSLR samples (i.e. 180 DSLR anomaly voxel *x,y,z* locations) remaining after the DSLR domain labeling, the ratio of anomalous to nominal samples was set to 1:4, each feature matrix was then $n_{total} = 900$ comprising 180 anomalous samples and 720 nominal samples (i.e. 900 DSLR voxel *x,y,z* locations). This was selected so that in any four-fold cross-validation model training using only a single feature matrix, the number of samples (¾ of 900) outnumbered the number of features ($F_n = 147.$). Nominal samples were chosen randomly from the set of 1600 nominal DSLR voxels which were down-sampled during the coordinate transformation from the $n_n = 6000$ nominal CT voxels.

4.3 Examination of Nominal and Anomaly DSLR Labels and Images

Examination of DSLR anomaly label locations can provide insight into the belief that machine learning is needed for binary classification using build layer images. Figures 4.7 and 4.8 contain images of an anomaly and nominal samples, respectively,

in a CT (80 x 80 CT voxels), post-fusion flash module 6 (25 x 25 DSLR voxels) and powder-recoating flash module 3 image for the previous build layer, instant build layer, and following build layer, with the center voxel in each instant build layer image corresponding to the sample's *x,y,z* location. A feature extraction filter outline is placed in all images, which represents the DSLR features extracted for machine learning from the displayed flash modules; the CT image has a mock feature extraction filter centered on the *x,y,z* location of the sample in the CT domain, obtained through the image processing. DSLR features from all flash module image stacks for an anomaly and nominal DSLR sample used for machine learning are displayed in Appendix A and B respectively for the anomaly and nominal samples displayed in figures 4.7 and 4.8.

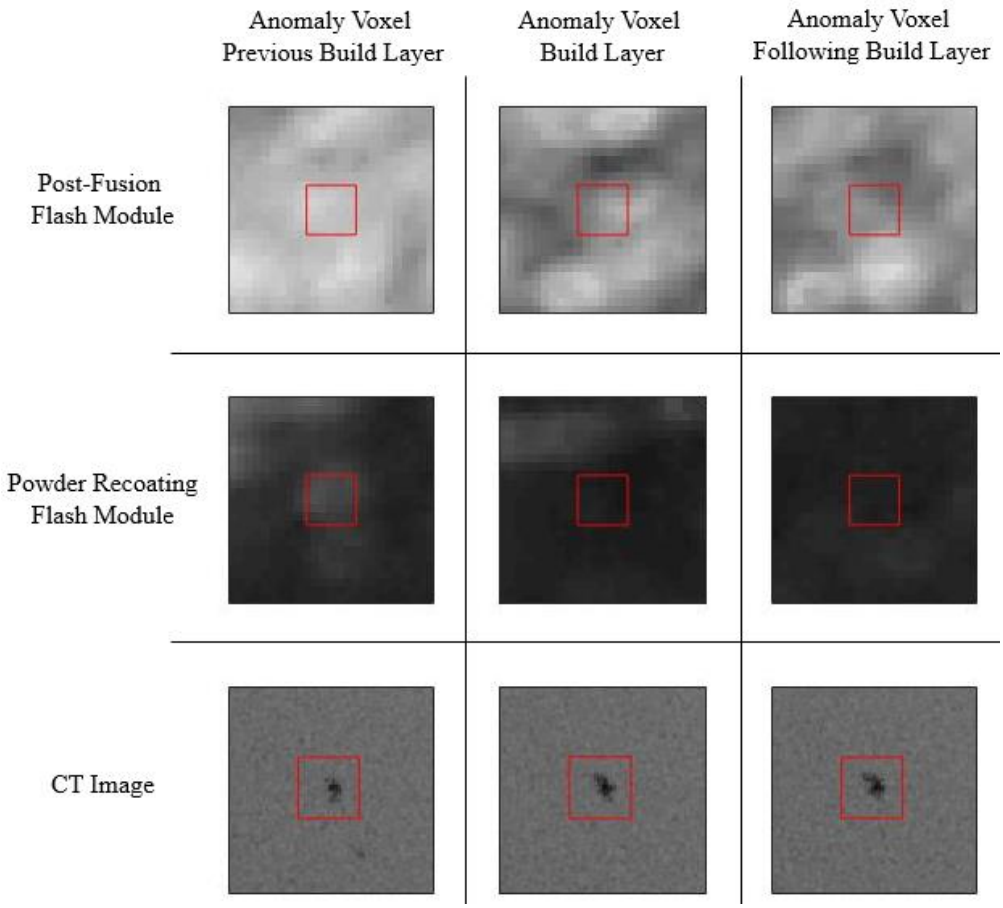

Figure 4.7 Anomaly label depicted in three builds layers of two flash modules and CT image with the respective feature extraction filter in red

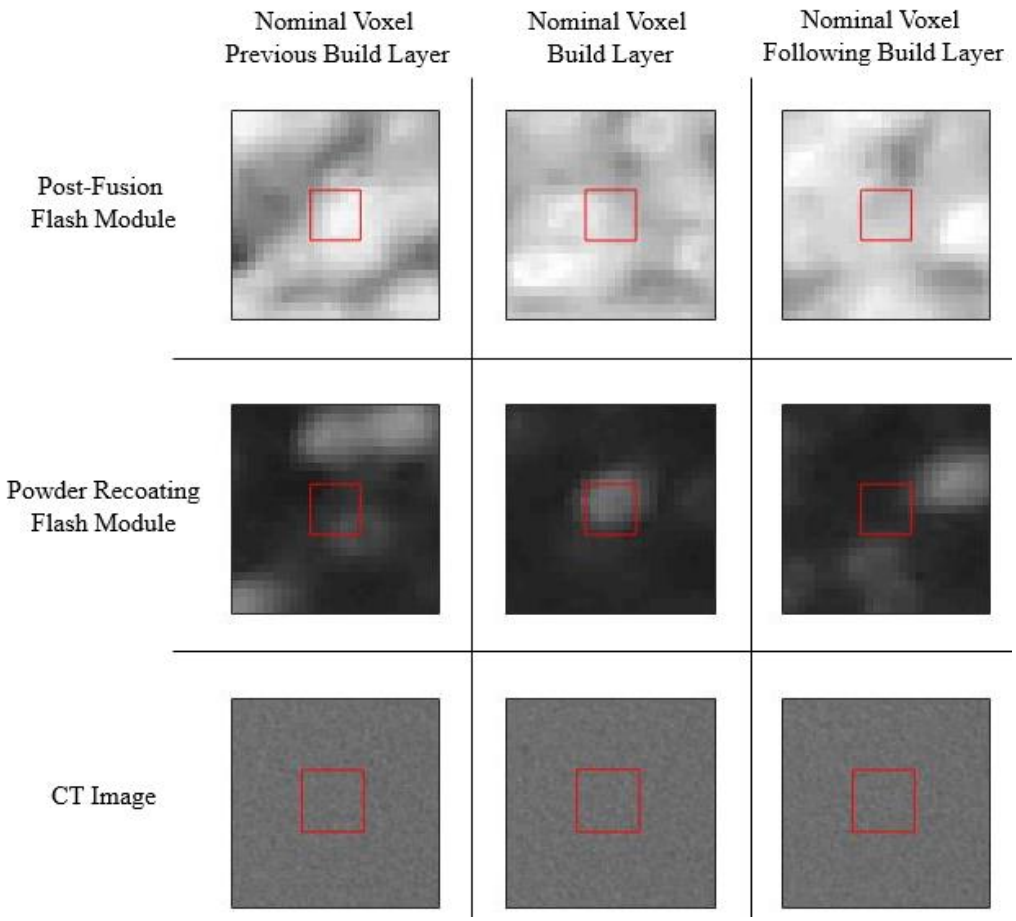

Figure 4.8 Nominal label depicted in three builds layers of two flash modules and CT image with the respective feature extraction filter in red

CHAPTER 5 Machine Learning in PBFAM Discontinuity Detection

5.1 Methodology of SVMs in Discontinuity Detection

SVMs historically have been applied to computer vision and text categorization problems, generalize well for unseen data and are relatively easy to implement [33]. In this investigation, supervised linear SVMs were employed in two discontinuity detection methodologies: (i) an ensemble classifier, being a linear SVM, which fused the signed distance to hyperplane values from eight linear SVM classifiers trained separately on each individual feature matrix and (ii) a single linear SVM was trained using all the feature matrixes at once.

The motivation to generate a discontinuity detection as in (i) was to avoid a scenario as in (ii) where the number of samples was less than the number of features during model training. The ensemble SVM discontinuity detection model in (i) circumvents the high dimensionality associated with the large feature extraction filters and number of feature matrices by fusing decisions of SVM models made in lower dimensions. Waske *et al.* [34] demonstrated that in a multiclass and multi-sensory data scenario, ensemble classifiers could outperform a single SVM classifier. Additionally, examining the ensemble decision fusion process would offer a machine defined discriminatory ability of each feature matrix flash module, in terms of SVM model parameters.

Alonso *et al.* [35] demonstrated the performance of SVM models on increasingly higher dimensional noiseless hyperspectral image data, noting that performance increased with increasing dimensionality, this is somewhat contrary to [34]. It was interpreted that a single SVM classifier in a large feature space as in (ii)

would benefit from the increased sparsity of data in a feature space comprising of all feature matrices, and therefore a better opportunity machine learning discontinuity detection. However a model created as in (ii) would be prone to the increased likelihood of overfitting, than compared to a model in (i).

The validation and reliability of both discontinuity detection methodologies is rooted in verifying performances of each methodology using a cross-validation experiment, robustness analysis in the face of added signal noise and similar margin separation [32]. Assessment of these metrics would make it observable if nominal and anomaly DSLR voxels are separable using machine learning as suspected.

5.2 SVMs, Ensemble Classification, and Performance Analysis

5.2.1 SVMs

Introduction for the linear SVM is presented in a manner similar to the implementation as in methodology (i), where a eight linear SVMs were trained on the eight feature matrices (i.e. a linear SVM model is explained using feature vectors from a single feature matrix). The fusion process of multiple SVMs is described in the next section 5.2.2.

A linear SVM inserts a maximum margin separating hyperplane in a feature space of $\mathbb{R}^d$, d =147, to best separate a set of L = 900 samples of $\vec{x}_{fi} \in \mathbb{R}^d$ with corresponding class labels $y_i \in \{-1,1\}$ for $i = 1,2,\dots,900$ [37]. Where $f = 1,2,\dots,8$ represents eight individually trained linear SVMS and associated model parameters. The hyperplane is defined as

$$0 = \overrightarrow{w_f}^T \vec{x} - b_f \tag{20}$$

where $\overrightarrow{w_f} \in \mathbb{R}^d$ is the normal vector of the hyperplane, $b_f \in \mathbb{R}$ is the bias and $b_f / \|\overrightarrow{w_f}\|$ determines the offset of the hyperplane from the origin along the normal vector. For cases that are linearly separable, called *hard margin*, the maximum margin separating hyperplane is found by minimizing $\|\vec{w}\|$ from (20) subject to

$$y_i\left(\overrightarrow{w_f}^T \vec{x}_{fi} - b_f\right) \geq 1) \text{ for } i = 1,2,\ldots,900 \text{ and } f = 1,2,\ldots,8 \tag{21}$$

The maximum margin hyperplane is completely determined by the $\vec{x}_{fi}$ which lie closet to the hyperplane, denoted as support vectors, which lie on two hyperplanes

$$+1 = \overrightarrow{w_f}^T \vec{x} - b_f \tag{22}$$

$$-1 = \overrightarrow{w_f}^T \vec{x} - b_f \tag{23}$$

which are parallel to the maximum margin separating hyperplane. A linearly separable case is shown in the figure 5.1, with 3 support vectors.

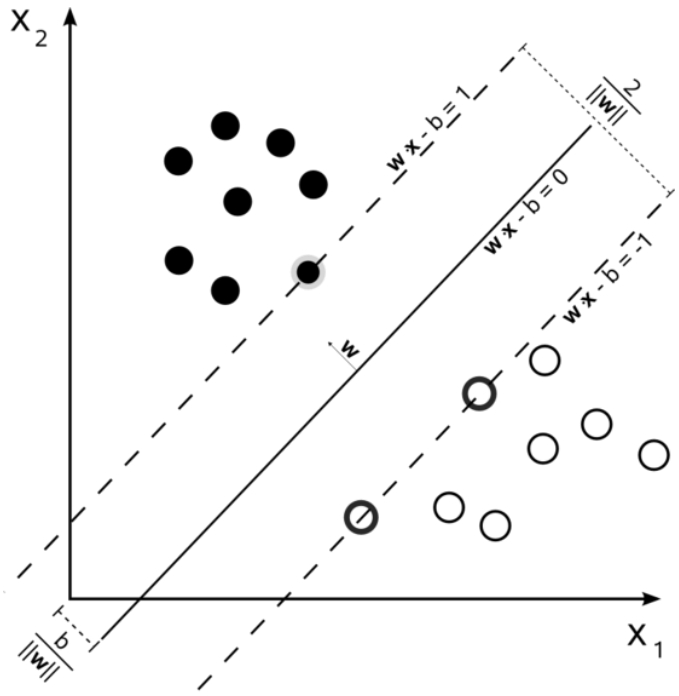

Figure 5.1 Example of separating hyperplanes as part of a SVM. (Source [36])

A hinge loss function is introduced for data which are not linearly separable (denoted as *soft margin*) defined as

$$\max(0, 1 - y_i(\overrightarrow{w_f}^T \vec{x}_{fi} - b_f)) \tag{24}$$

Where (24) is equal to 0 for $\vec{x}_{fi}$ on the correct side of the margin or if $\vec{x}_{fi}$ lie on the wrong side of the margin then (25) is equal to the proportional distance between $\vec{x}_{fi}$ and the margin [37]. $\|\overrightarrow{w_f}\|$ and b_f are then determined by minimizing

$$J = \left[\frac{1}{L}\sum_{i=1}^{L} \max\left(0, 1 - y_i\left(\overrightarrow{w_f}^T \vec{x}_{fi} - b_f\right)\right)\right] + \lambda\|\overrightarrow{w_f}\|^2 \tag{25}$$

Where λ determines the tradeoff between increasing margin size and ensuring that the $\vec{x}_i$ lie on the correct side of the margin; small values of λ make the soft-margin SVM behave as a hard-margin SVM. A trained linear SVM model is

$$\hat{L} = sgn(\overrightarrow{w_f}^T \vec{x}_{fi} - b_f) \tag{26}$$

where (26) assigns either -1 or +1 for model classification. Additionally, a sample's signed distance to hyperplane can be calculated as

$$d(\vec{x}_{fi}) = \frac{\overrightarrow{w_f}^T \vec{x}_{fi} - b_f}{\|\overrightarrow{w_f}\|} \tag{27}$$

where large absolute values of $d(\vec{x}_{fi})$ represent points furthest from the hyperplane, which is positive on one side and negative on the other (i.e. the classification from (26)). Comparing the model output $\hat{L}_i \in \{-1, +1\}$ for any $\vec{x}_{fi}$ to is used to assess and supervise the machine learning process. In this investigation, multiple SVMs were trained and evaluated using the MATLAB function *svmtrain* to generate a model's $\overrightarrow{w_f}$, and b_f parameters.

The methodology as described in (ii), i.e. a single SVM classifier, separated anomaly and nominal conditions in a $F_n = 1176$ dimensional feature space (comprising features from all 8 flash modules simultaneously) whereby a linear SVM was trained

on the concatenated feature vectors of samples $\vec{x}_{fi}$ from all $f = 1,2,\ldots,8$, feature matrices with model parameter outputs $\overrightarrow{w_s}^T$ and b_s.

5.2.2 Ensemble Classification with SVMs

An ensemble classifier uses a combination of classifier outputs to create a single decision and is again discussed before a cross-validation experiment is implemented. This investigation employed an ensemble classification scheme where a linear SVM model was trained on each individual feature matrix M_f, corresponding to each individual flash module and thus creating eight models which separated anomaly and nominal conditions in each individual $F_n = 147$ dimensional feature space (as described in the previous section). The final ensemble SVM classifier was given the signed distance to hyperplane values, $d(\vec{x}_{fi})$ for each sample from each feature matrix M_f SVM classifier, stored in the ensemble feature matrix, F_E, where $n_{total} = 900$ and $V = 8$.

$$F_E \in \mathbb{R}^{n_{total} \times V} \tag{28}$$

Using the ensemble feature matrix, an additional linear SVM (the ensemble SVM classifier) is trained on the eight signed distance to hyperplane values obtained from the eight linear SVMs trained on each feature matrix. Where $\vec{e}_i \in \mathbb{R}^{\mathrm{V}}$, is made up of eight $d(\vec{x}_{fi})$ from each individual SVM with $y_i \in \{-1,1\}$ for $i = 1,2,\ldots,900$ and $f = 1,2,\ldots,8$

$$sgn(\overrightarrow{w_e}^T \vec{e}_i - b_e) \tag{29}$$

This process of fusion for the ensemble classification scheme is depicted in figure 5.2.

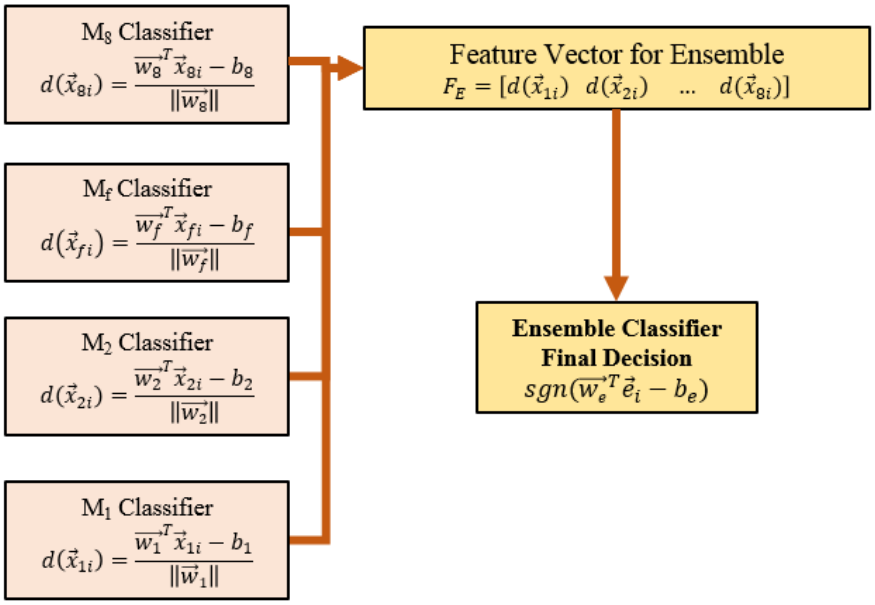

Figure 5.2 Ensemble Classification Scheme.

5.2.3 Cross-validation and Performance Evaluation

The single SVM and ensemble classifier discontinuity detection model performances were assessed in a four-fold cross-validation experiment, whereby the data was divided into four subsets using equalized sampling (i.e. each subset contained an equal number nominal and anomalous samples). Each subset was tested with a model generated by the remaining three subsets which acted as training data for the model. This was repeated for each subset.

Performance was formally assessed using accuracy, recall, and precision calculated for each subset defined as

$$Accuracy = \frac{\sum True\ positive + True\ Negative}{\sum Total\ Population} \tag{30}$$

$$Recall = \frac{\sum True\ positive}{\sum Condition\ positive} \tag{31}$$

$$Precision = \frac{\sum True\ positive}{\sum Test\ Outcome\ Positive} \quad (32)$$

Where: true positives are anomalous samples, properly classified as anomalous samples; true negatives are nominal samples, properly classified as nominal samples; false negative are anomalous samples classified (incorrectly) as nominal; false positives are nominal samples classified (incorrectly) as anomalous; test outcome positives are samples classified as anomalies (true positives + false positives); and condition positives are anomalous samples (true positive + false negative). In this investigation, it is crucial for the accuracy metric to be above 50%, this threshold is the boundary which would indicate successful machine learning.

Performance of both discontinuity anomaly detection models was analyzed with respect to DSLR anomaly cluster size and signed distance to DSLR anomaly cluster centroids. Disregarding cluster assignment represents a machine learning standard for rigorous classification performance, while including cluster assignment mimics a methodology more meaningful in an industrial setting where identification of discontinuities is desired, where mitigation of identified discontinuities would involve designating the surrounding local region of the detected anomaly DSLR voxel for corrective action. In a further analysis, including cluster assignment for discontinuity detection meant that if a single anomaly DSLR voxel belonging to a cluster was detected then the entire cluster of anomaly DSLR voxels was detected as well, a strategy appropriate for real applications.

For each discontinuity detection model, signed distance to hyperplane values were compared between the cross-validated models to ensure similar separation between anomaly and nominal conditions. For each set of signed distance to hyperplane

values created per cross-validated model and discontinuity detection method, values were standardized to compare both discontinuity detection methodologies.

A receiver operating characteristic (ROC) curve was generated for each cross-validated model. ROC curves display the performance of a binary classifier as the discrimination threshold is varied (i.e. the separating hyperplane is shifted along the normal vector), plotting the true positive rate (i.e. recall) vs the false positive rate (false positives divided by number of condition negatives) at various threshold settings. Similar performance between cross-validated models in a ROC plot is desired, indicating similar discrimination between models and no overfitting.

Noise was added to the testing data for the cross-validated models to assess the robustness of both discontinuity detection methodologies and the similarity between cross-validated models. For each subset of test data, feature dimensions for each sample were added with a randomly selected intensity scalar value from a set of standardized normally distributed scalar values between [+1, -1]. Noise was increased by scaling the set of normally distributed scalars value by a noise variable P. Model performance metrics for accuracy, recall and precision were recorded as noise P was increased from 1 to 30. With added noise, no feature vector had a value greater that of 255 gray scale intensity, the maximum for the DSLR camera in this investigation. Figure 3.5 displays an image from flash module 6 with added noise at P = 30.

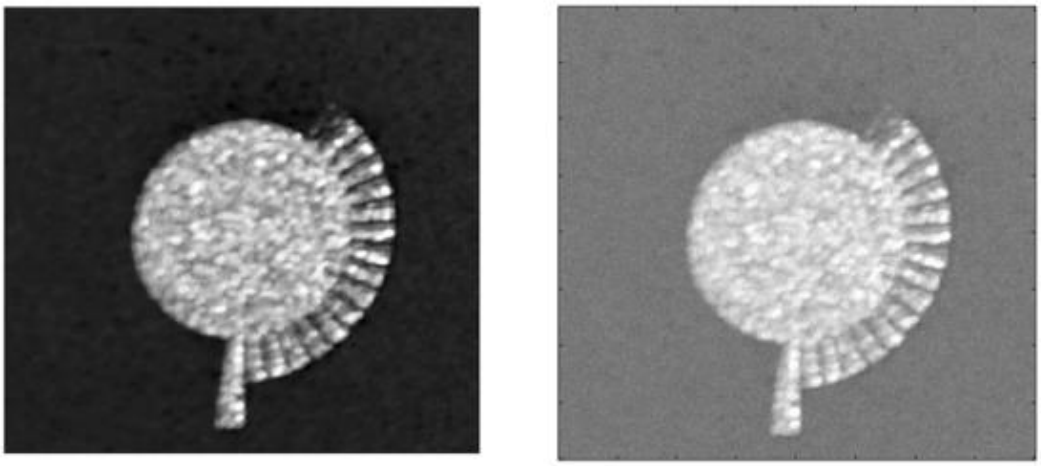

Figure 5.3 Flash module 6 image (left) with added noise at P = 30 (right).

5.3 Evaluation of SVM Ensemble Discontinuity Detection

5.3.1 Ensemble Model Performance

Classification results for accuracy, recall and precision, using equations (30), (31) and (32) are displayed in table 5.1, defined in terms of average value ± one standard deviation cumulated over the four-fold cross-validation models. The results shown in table 5.1 are for each individual feature matrix linear SVM classifier and the ensemble linear SVM classifier.

Table 5.1 Average value and standard deviations of accuracy, precision and recall for each feature matrix SVM classifier and ensemble classifier.

Feature matrix of flash model	Mean Accuracy ± 1 Std. Dev.	Mean Precision ± 1 Std. Dev.	Mean Recall ± 1 Std. Dev.
1	*72* ± 1.2 %	37 ± 1.5 %	42 ± 4.9 %
2	*62* ± 2.3 %	24 ± 5.1 %	53 ± 12.1 %
3	*71* ± 3.4 %	35 ± 4.4 %	55 ± 2.3 %
4	*66* ± 4.2 %	31 ± 4.9 %	55 ± 10.5 %
5	*63* ± 5.8 %	27 ± 5.2 %	51 ± 10.0 %
6	*73* ± 4.2 %	39 ± 4.7 %	63 ± 8.3 %
7	*64* ± 4.9 %	29 ± 4.2 %	54 ± 2.3 %
8	*68* ± 0.8 %	33 ± 2.2 %	60 ± 7.9 %
Ensemble Classifier	86 ± 0.9 %	66 ± 1.8 %	68 ± 4.2 %

Accuracy for the ensemble classifier above 50% demonstrated the ability of the ensemble classifier to discriminate discontinuities using layerwise images. Similar performance of cross-validated models, represented by the small standard deviation, indicates consistent performance for the SVM classifiers across each fold, but not necessarily identical models. Implementation of an ensemble classifier achieved ~86% accuracy compared to the individual flash module classifiers ranging from 63%–73%. The low precision and recall of the individual flash module classifiers was greatly improved upon in the ensemble classifier, indicating that (at least a portion of) the 8 flash modules did, indeed, provide additional useful information for this purpose.

Figure 5.4 displays the total number of DSLR voxels per cluster size class along with the total number of true positive DSLR voxels for each cluster size class from all four testing sets of the cross-validation folds. Figure 5.4 is representative of the table 5.1 recall and rigorous machine learning classification techniques.

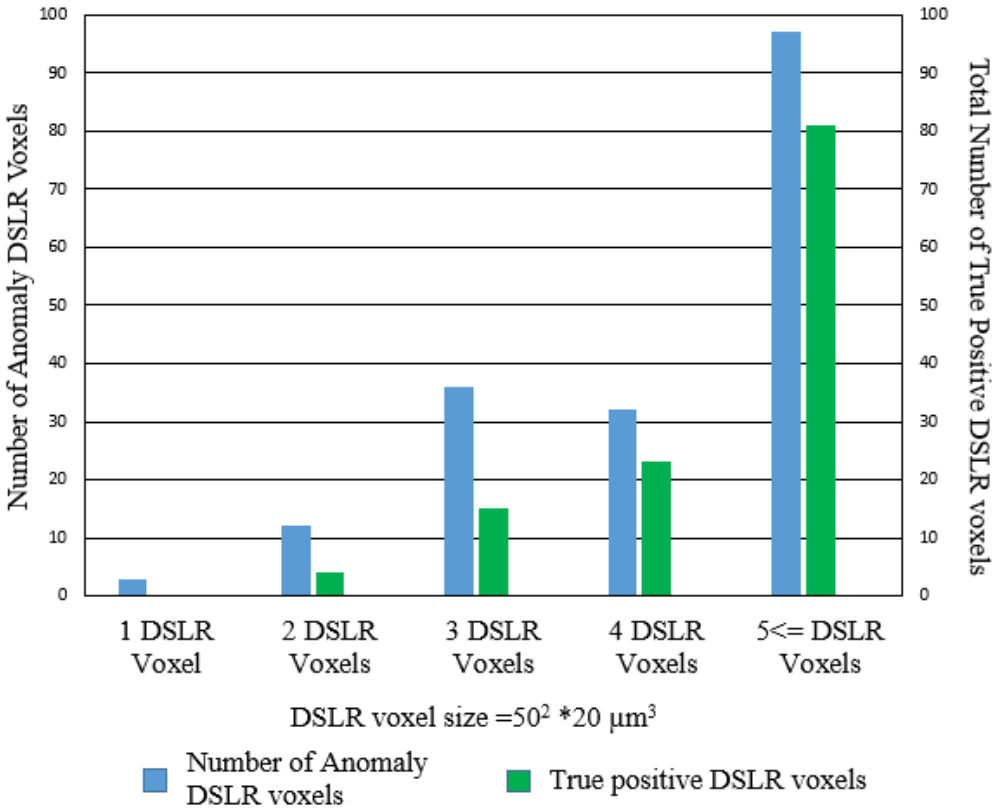

Figure 5.4 Frequency of condition positive (blue – left axis) and true positive (green – right axis) DSLR anomalies with respect to DSLR cluster size for ensemble classification.

Figure 5.5 displays the frequency of each cluster size class in the DSLR domain along with total number of successfully detected anomaly clusters, whereby a DSLR anomaly cluster was detected if any of the belonging DSLR anomaly voxels were detected, mimicking an industrial application for discontinuity detection with the intent of subsequent *in situ* mitigation.

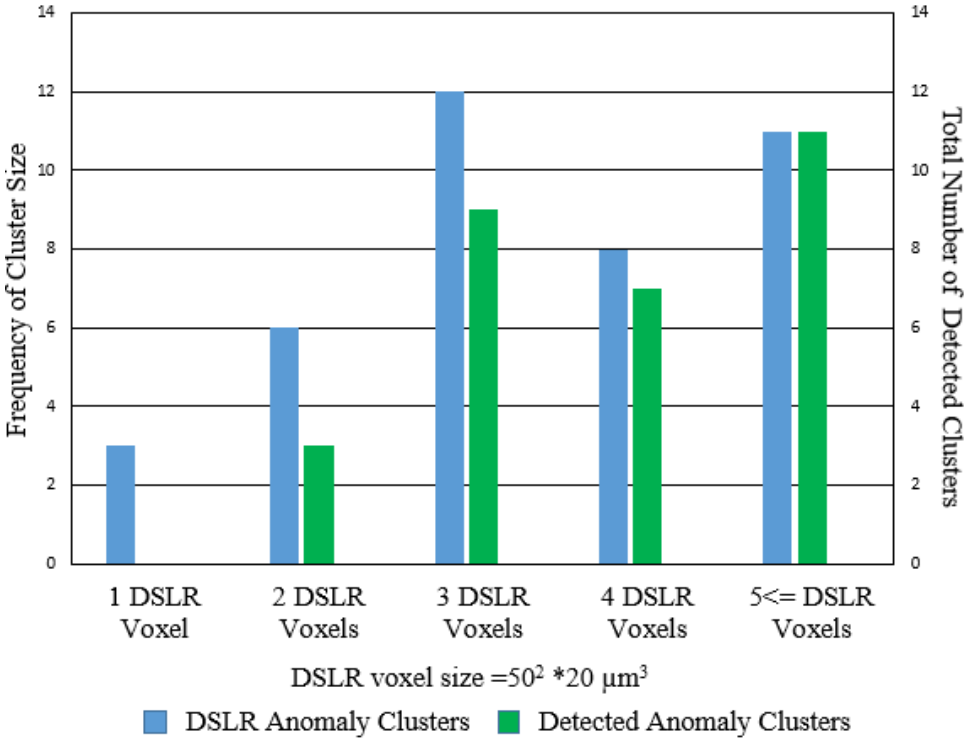

Figure 5.5 Frequency of cluster size (blue – left axis) and detected clusters (green - right axis) per DSLR cluster size of the ensemble classifier.

In both figures 5.4 and 5.5 it has been demonstrated that DSLR voxels pertaining to larger anomaly DSLR clusters are detected more easily (i.e. more separable from nominal conditions). Table 5.2 displays the recall of the ensemble classifier with respect X, Y and Z displacement to cluster centroid. From table 5.2 recall is shown to vary across all displacement to cluster centroid values, however does agree that larger anomaly clusters are easier to detect.

Table 5.2 Ensemble classification recall with respect to voxel displacement to anomaly cluster centroid.

DSLR Voxel Displacement to Anomaly Cluster Centroid	Z Axis	X Axis	Y Axis
-2	100%	n/a	66%
-1	57%	60%	83%
0	73%	63%	60%
1	50%	80%	79%
2	100%	100%	50%

Signed distance to hyperplane values were generated and standardized within each cross-validated model to validate that each cross-validation model identified similar separation margins. Figure 5.6 displays a histogram for the standardized signed distance to hyperplane values for the ensemble fusion separating hyperplane per cross-validated model.

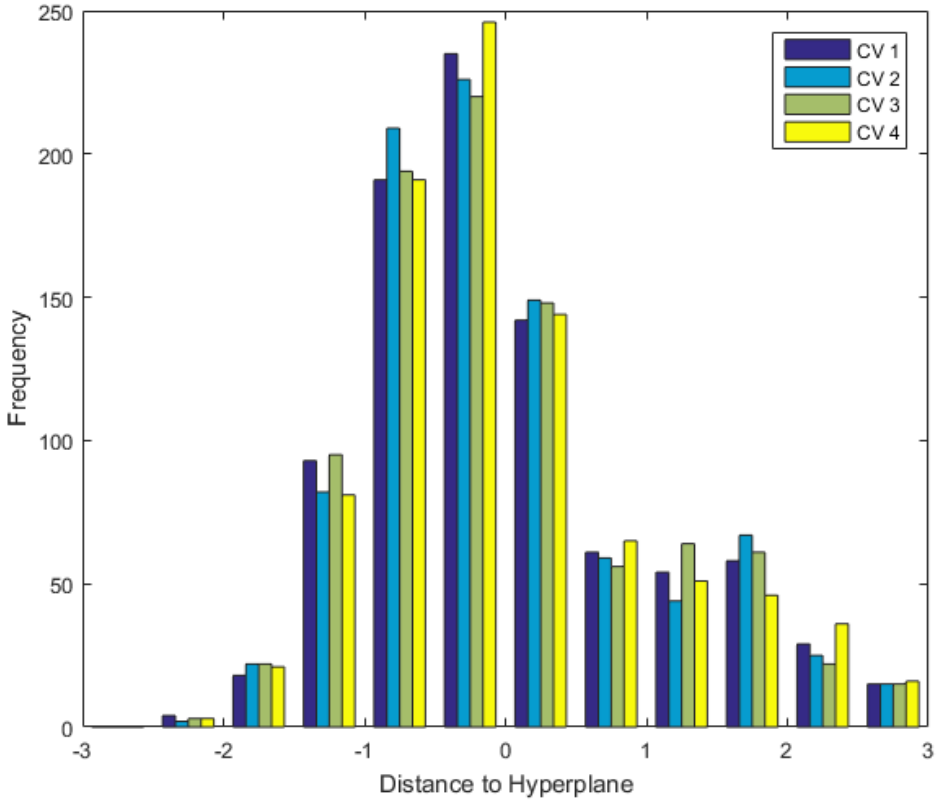

Figure 5.6 Standardized signed distance to hyperplane values for the ensemble SVM classifier.

Figure 5.6 illustrates similar separation between each cross validated model. Average variance for each sample's signed distance to hyperplane values were for anomaly DSLR voxels 0.2502, and for nominal DSLR voxels was 0.0986. The low average variance and similar displays in figure 5.6 histogram indicate similar separation.

Figure 5.7 displays the ROC curves for the four cross-validation folds, indicating a discriminatory ability of the ensemble model between anomaly and nominal DSLR voxels. The consistent performance of all four cross-validated models across the scope of the ROC curve in figure 5.7 indicates that each cross-validated model identified similar discriminatory margins.

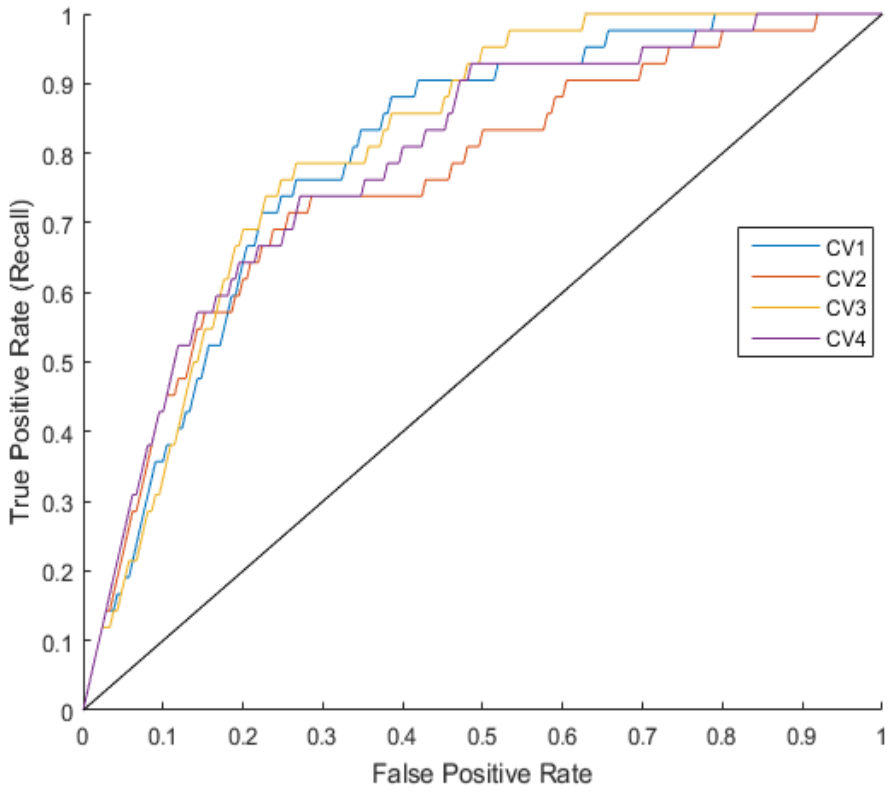

Figure 5.7 ROC curve for ensemble classifier cross-validated models.

The ensemble classifier's fusion of the individual flash module SVMs, and individual performance characteristics presented in table 5.1, can be used to rate the effectiveness of each individual flash module. Table 5.3 displays the average value ± one standard deviation cumulated over the four-fold cross-validation models of the elements of the model parameter $\overrightarrow{w_e}$. A larger value of $\overrightarrow{w_e}$ signifies greater discriminatory contribution of a flash module SVM.

Table 5.3 SVM model parameters from ensemble cross-validation.

SVM model of flash module	Mean $\overrightarrow{w_e}$ ± 1 Std. Dev.
1	2.80 ± .28
2	2.03 ± .36
3	2.16 ± .35
4	3.34 ± .12
5	2.07 ± .38
6	2.68 ± .54
7	1.47 ± .55
8	2.30 ± .46

Examining table 5.1 performance characteristics and table 5.3, $\overrightarrow{w_e}$ parameter values of flash modules it is evident that flash modules 1, 3, 4 and 6 stand out; these flash modules have large accuracies and $\overrightarrow{w_e}$ coefficients. Furthermore, ensemble false positive anomaly DSLR voxels were misclassified by 5.07 ± 1.19 ($\mu \pm 1\ \sigma$) individual flash module SVMs; ensemble true positives anomaly DSLR voxels were misclassified by 1.63 ± 1.58 individual flash module SVMs; ensemble false negative nominal DSLR voxels were misclassified by 4.43 ± .97 individual flash module SVMs; and ensemble true negative nominal DSLR voxels were misclassified by 2.16 ± 1.23 individual flash module SVMs. From these results, it can be inferred at least 5 flash module images are needed to provide that best opportunity to make discriminatory decisions.

5.3.2 Robust Analysis of Ensemble Model

In order to assess the robustness of the machine learning models in presence of noise, noise was only added to feature vectors of the individual flash module SVMs, and not the signed distance to hyperplane values for the ensemble classifier, effectively representing only noise added during data collection which is similar to added noise in the gray scale images. Noise added into the signed distance to hyperplane values for the ensemble classifier may or may not be representative of noise expected in a real application. Figure 5.8 displays accuracy, precision and recall of the cross-validated single SVM models as a function of the added Gaussian noise scaled pixel intensity value P ranging from 1 to 30. At each P value a rectangular box encompasses the range of metric values for the cross validated models, where a smaller box indicates similar metric performance between cross validated models.

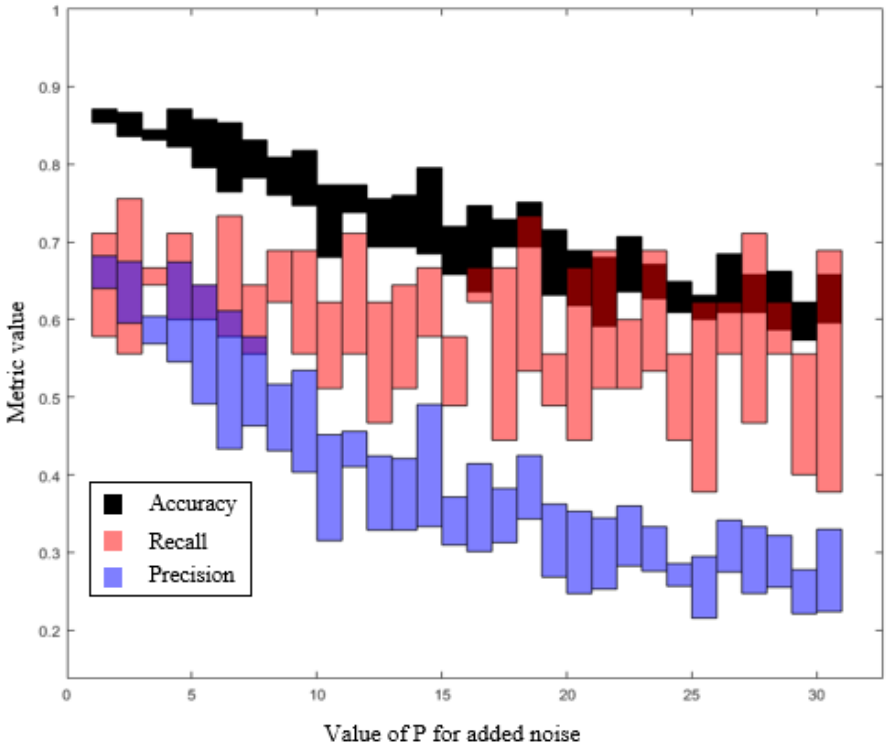

Figure 5.8 Robust analysis of ensemble SVM discontinuity detection strategy displaying range of metric values for each value of P.

5.4 Evaluation of Single SVM Discontinuity Detection

5.4.1 Single SVM Model Performance and Validation

Classification results for accuracy, recall and precision, using equations (30), (31) and (32) for the single SVM classifier are displayed in table 5.4, defined in terms of average value ± one standard deviation cumulated over the four-fold cross-validation models.

Table 5.4 Performance metrics for the ensemble classifier and single SVM classifier.

Classifier	Mean Accuracy ± 1 Std. Dev.	Mean Precision ± 1 Std. Dev.	Mean Recall ± 1 Std. Dev.
Single SVM	89 ± 2.7 %	73 ± 7.9 %	74 ± 4.2 %

Performance of the single SVM in the cross-validation experiment shows the ability to discriminate between anomalies and nominal, with average accuracy at 89% above the 50% threshold. Figure 5.9 displays the single SVM recall with respect to anomaly cluster size. Figure 5.10 displays the frequency of each cluster size class in the DSLR domain along with total number of successfully detected anomaly clusters, again a DSLR anomaly cluster was detected if any of the belonging DSLR anomaly voxels were detected.

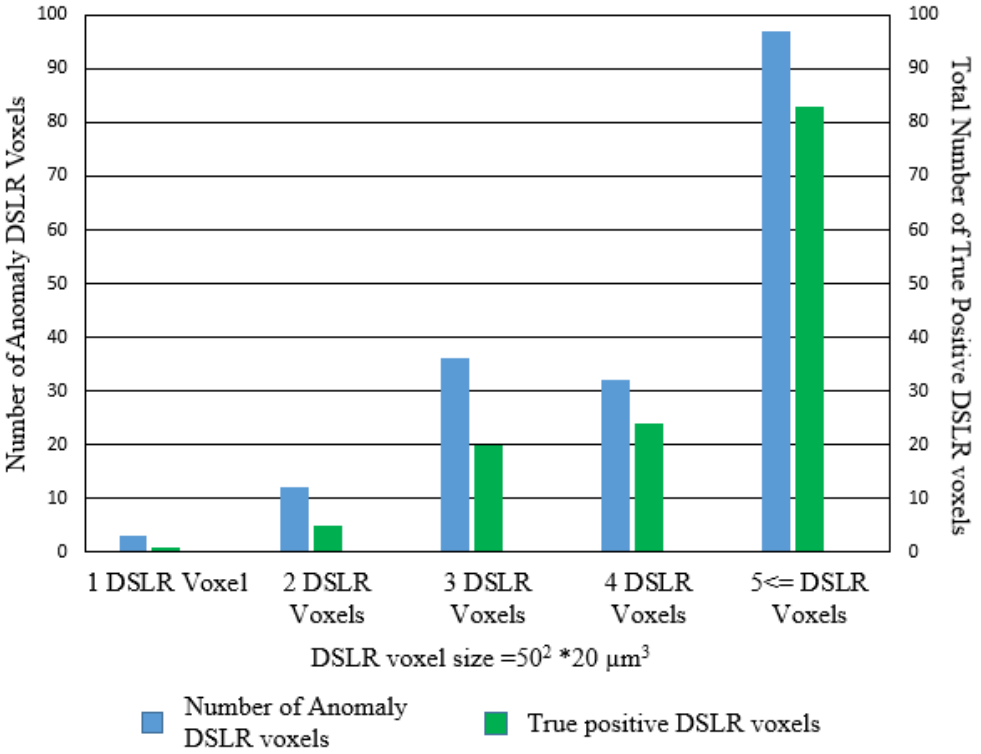

Figure 5.9 Frequency of condition positive (blue – left axis) and true positive (green – right axis) DSLR anomalies with respect to DSLR cluster size of the single SVM.

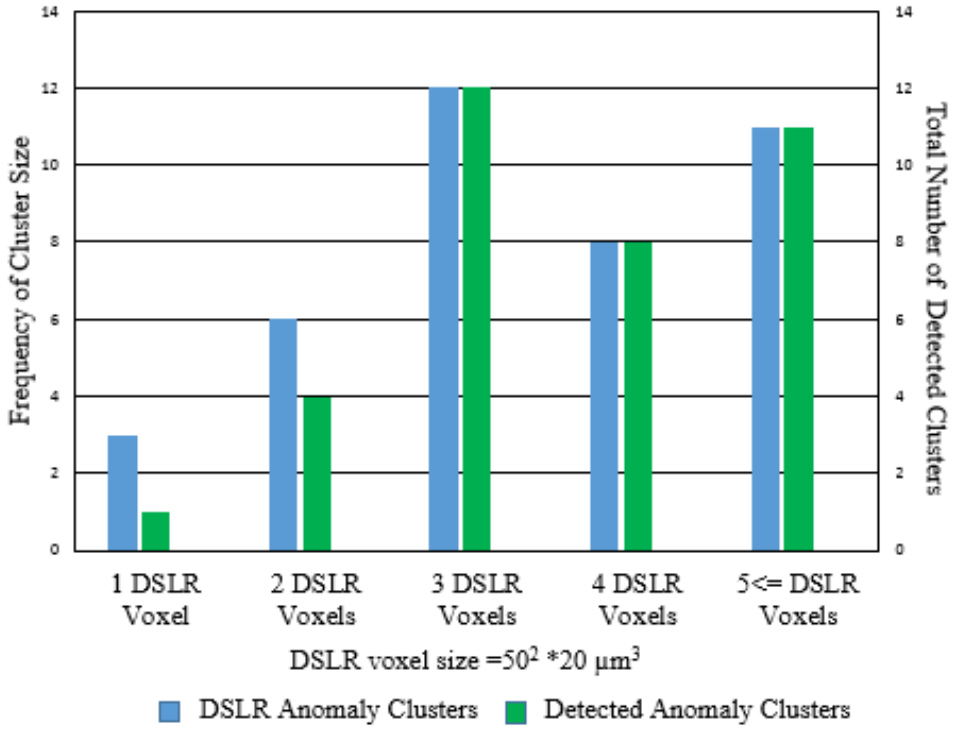

Figure 5.10 Frequency of cluster size (blue – left axis) and detected clusters (green – right axis) per DSLR cluster size of the single SVM.

In both figures 5.9 and 5.10 it has been shown that larger DSLR anomaly clusters are easier to discriminate, just as in the ensemble classifier. Figure 5.10 demonstrates that DSLR anomaly clusters larger than 2 DSLR anomaly cluster were detected 100% of the time. Table 5.5 displays the recall of the ensemble classifier with respect X, Y and Z distances to cluster centroid.

Table 5.5 Single SVM classification recall with respect to voxel displacement to anomaly cluster centroid.

DSLR Voxel Displacement to Anomaly Cluster Centroid	Z Axis	X Axis	Y Axis
-2	80%	n/a	66%
-1	62%	87%	88%
0	83%	68%	58%
1	40%	87%	71%
+2	100%	100%	100%

Signed distance to hyperplanes were generated for each single SVM cross-validated model and standardized, displayed in figure 5.11.

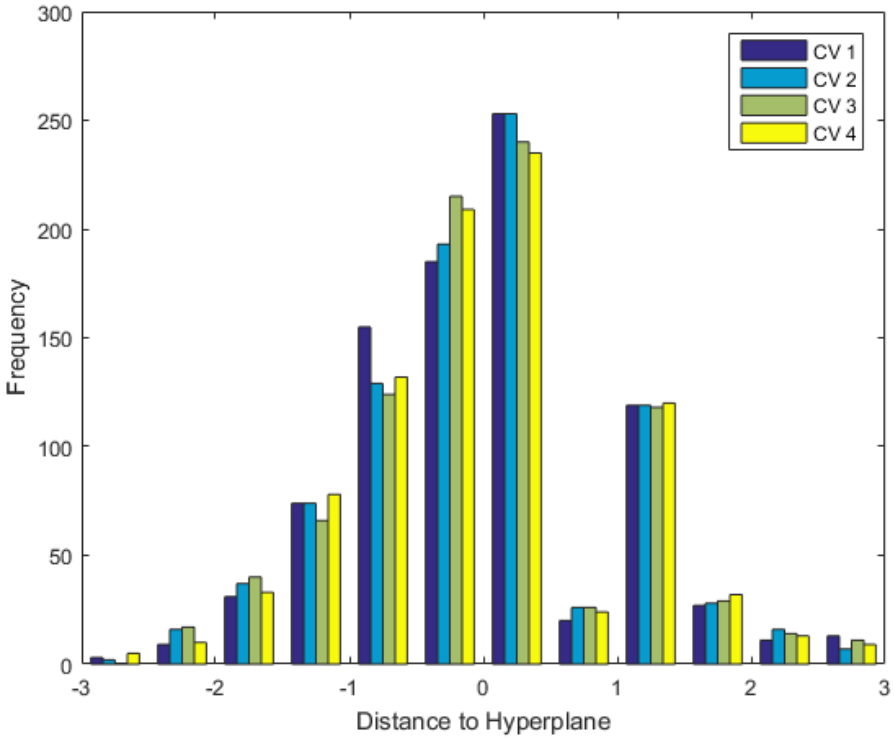

Figure 5.11 Standardized signed distance to hyperplane values for single SVM cross-validated models.

Average variance for each sample's signed distance to hyperplane values for anomaly DSLR voxels was 0.167 and for nominal DSLR voxels was 0.113. Similarity between cross-validated models in figure 5.11 and a small average variance for the DSLR voxel signed distance to hyperplane values demonstrates similar separation between anomaly and nominal DSLR voxels. Figure 5.11 also displays the bi-modal distribution of nominal and anomaly DSLR voxels in the single SVM feature space, where classified anomaly DSLR voxels are positive and classified nominal DSLR voxels are negative.

Figure 5.12 displays the ROC curves for the four cross-validation folds, indicating a similar discriminatory ability between the ensemble cross-validated models across the scope of the ROC graph.

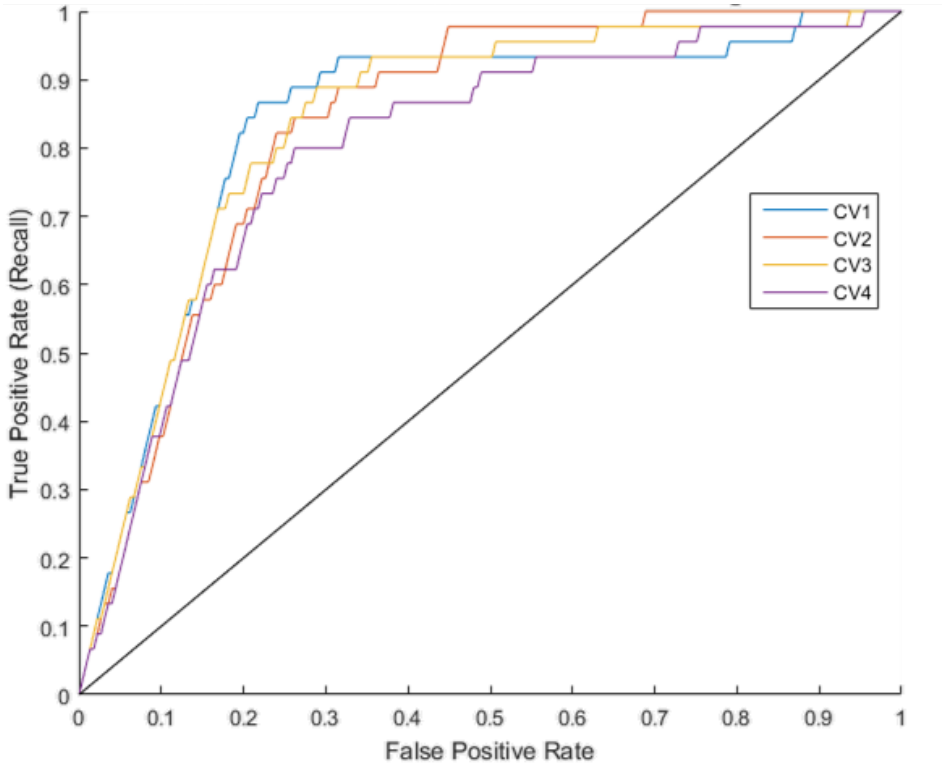

Figure 5.12 ROC curve for single SVM classifier cross-validated models.

5.4.2 Robust Analysis of Single SVM Model

In a similar fashion to section 5.3.3 the single SVM performance was monitored with increasing added noise to the data set. Figure 5.13 displays accuracy, precision and recall of the cross-validated single SVM models as a function of added Gaussian noise scaled pixel intensity value ranging from P = [1:30]. At each P a rectangular box encompasses the range the range of metric values for the cross validated models, where a smaller box indicates similar metric performance between cross validated models.

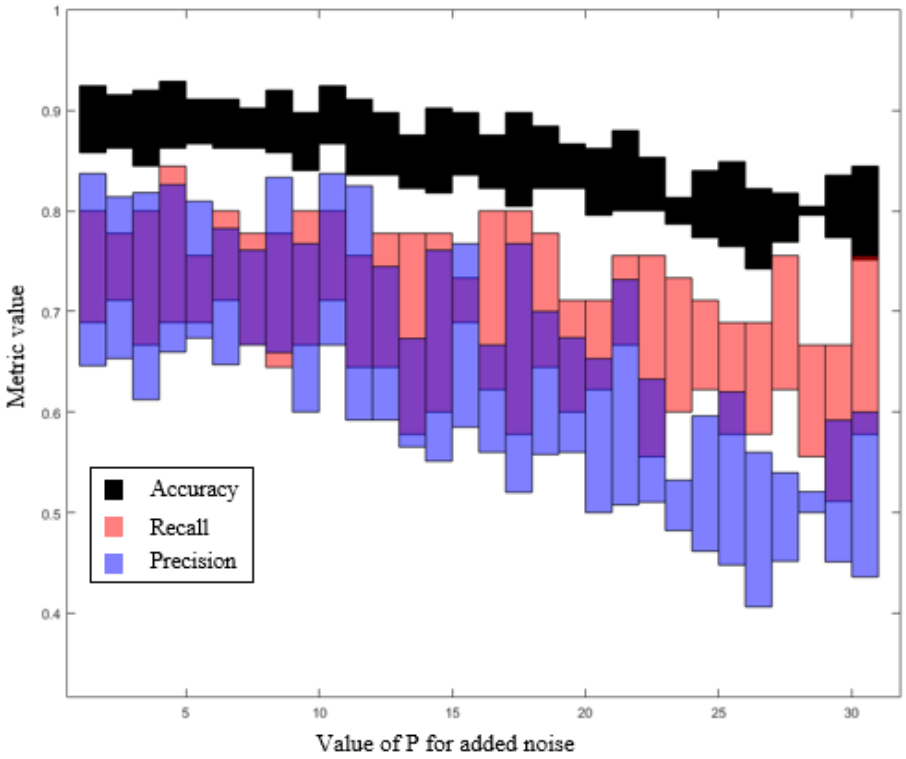

Figure 5.13 Robust analysis of single SVM discontinuity detection strategy displaying range of metric values for each value of P.

The consistent accuracy of the model across the range of added noise indicates that the cross-validated models separated the data in a similar manner. Across the range of added noise, the accuracy of cross-validated single SVM classifiers failed to completely fall below 50%.

CHAPTER 6 CONCLUSION

6.1 Assessment of Discontinuity Detection Scheme

Image processing techniques employed in 3 dimensions using multiple layers of CT images provided an excellent tool for quantifying and locating part discontinuities for ground truth labels, enabling supervised machine learning of *in situ* data domains. As a non-destructive evaluation technique, CT scanning of AM parts provides an excellent way to characterize part quality and identify and locate individual flaws in *x,y,z* space, enabling the data to be employed as a ground truth for labeling regions of AM parts to be used in training machine learning algorithms. However, the discretization of the CT domain limits the minimum size of detectable discontinuities that can be identified. In this investigation, it was recognized that it is only necessary to identify ground truth labels belonging to anomaly CT clusters with a specified minimum size, and performing automated defect detection below a set minimum anomaly size threshold would potentially enable noise in the CT images to interfere with the ground truth labeling of discontinuities.

Defining a feature extraction filter size in terms of coordinate transformation RMSE served to confidently state and know the accuracy with which the information pertaining to a ground truth label transferred into the DSLR images from the CT domain was captured by the feature extraction filter. Additionally, the reference points enable any *in situ* visual sensor to be labeled for a supervised machine learning process, and can be extended to use part perimeter coordinates, obtained via image processing techniques, as reference points to build a coordinate transformation.

The large feature extraction filter, an artifact of a non-exact coordinate transformation between sensor data and post-build CT scan data, was demonstrated to capture enough information for each label in the DSLR label to enable effective machine learning training. It is evident and known that the surrounding local regions of a labeled DSLR voxel (in three dimensions) can provide discriminatory information. Should a discontinuity detection scheme be incorporated into a production AM system, the area encompassed by a feature extraction filter of a detected anomaly *x,y,z* location would be slated for corrective action, i.e. re-melting. Machine learning performance, specifically the recall, of the discontinuity detection models rose significantly when it was assumed that the local region around a detected anomaly DSLR was identified as anomalous.

Parallel performances of cross-validated models in accuracy, precision and recall, ROC curves, and signed distance to hyperplane values, for each discontinuity detection methodology, demonstrated that indeed discontinuities identified in CT scan images can be effectively separated in *in situ* build-layer images using machine learning, with demonstrated 86% and 89% accuracy. The increased performance of the single SVM as compared to the ensemble SVM, attributed to the sparsity of data in the single SVM feature space, is desired but it cannot be overlooked that the sample size to feature space ratio is below one yielding sparse data representation, thus bringing the result into question.

Both discontinuity detection models, especially the ensemble classifier's performance increase from combining individual flash module SVMs, demonstrated that in order to make an informed decision on part quality, multiple images after powder

recoating and laser fusion under different lighting conditions should be used. Additionally, the ensemble separating hyperplane effectively rated the discriminatory ability of each flash module, where flash modules 1, 3, 4 and 6, being two post-fusion and powder coating flash modules, were the highest rated. This may enable identification of individual sensor modules that provide redundant-or-extraneous information and that can, thus, be eliminated.

6.2 Improvements and future work

It would be a valid assumption that an increase in camera resolution would ultimately lead to an increase in discontinuity detection performance when executed in a similar manner as presented. As noted current camera resolution is on the order of 50 µm pixel and of comparable scale to anticipated defect size. Higher resolution can be easily achieved by changing the view of the camera images to capture specific regions of the build plate, where (with current technology) additional cameras would be needed if the entire build plate was to be surveyed. It would also be a fair assumption to say that the resolution of commercially available cameras would increase over time as well, therefore only one camera could be used if desired.

An increase in camera resolution would enable the feature extraction filter to be sized more meaningfully, relative to anticipate flaw size. It is evident that the local region surrounding a discontinuity (in three dimensions) can provide discriminatory information, however in this investigation the minimum size of the feature extraction filter depended on the error of the coordinate transformation from CT to DSLR domain. In a scenario where the coordinate transformation error is minimized, the need to find the optimally sized feature extraction filter is crucial; too large of a filter will

lead to unnecessary data-processing, while a small feature extraction would diminish the performance of a discontinuity detection strategy. An experiment which demonstrates the performance of a discontinuity detection scheme as a function of feature extraction filter size would be ideal.

This investigation demonstrated visual sensing discontinuity detection with a limited data set (i.e. one test part at nominal conditions not including part edges). The feature extraction filters and machine learning models developed in this investigation would require enhancement in order to be effective at detecting discontinuities near part edges, as regions near the edge of AM-built parts are known to be prone to lack of fusion defects. Future work could include the creation of a library of information containing discriminatory information from parts built under varying environment settings which induce part errors, exposing a detection model to a range of possible discontinuities found in PBFAM parts. Ideally a discontinuity detection model would be trained from multiple builds and tested on a separate build, which would enable the generation of a generalized discontinuity detection model.

Implementing non-linear machine learning algorithms, such as neural networks and non-linear SVMs, could have the potential for increased classification performance as compared to the linear machine learning algorithms implemented in this investigation. Additionally, the machine learning infrastructure developed in this work lays the groundwork to supplement visual sensing-based discontinuity detection with data from other position-synchronized melt pool monitoring systems which monitor the melt pool process, or with melt pool simulation tools which predict part quality. Armed with this information, model parameters can be updated and improved once

confirmation of part quality can be made with an *in situ* visual sensor discontinuity detection.

A formal method is needed which uses a generated discontinuity detection scheme to grade part quality, a part can be rejected if it has been detected to contain too many discontinuities, which can then be confirmed via CT scan. Ultimately an investigation which builds a connection between online discontinuity detection part grading and mechanical part tests would be desired.

References

[1] ASTM Standard, Standard Terminology for Additive Manufacturing-General Principles-Terminology, ASTM F42 Committee, ASTM International, 2015.

[2] I. Gibson, D. W. Rosen, B. Stucker. Additive Manufacturing Technologies. Springer New York. 2010

[3] W. Gao, Y. Zhang, D. Ramanujan, K. Ramani, Y. Chen, C. Wang, Y. Shen, S. Zhang, P. Zavattieri, The status, challenges, and future of additive manufacturing in engineering, Computer-Aided Des. 69 (2016) 65-89.

[4] G. Tapia, A. Elwany, A review on process monitoring and control in metal-based additive manufacturing, J. Manuf. Sci. Eng. 136 (6) (2014) 60801–60811.

[5] J. Holmstrom. J Tuomi, J. Partanen. Rapid manufacturing in the spare parts supply chain: Alternative approaches to capacity deployment. Journal of Manufacturing Technology Management. 21 (2009) 687-697

[6] S. Mellor, L. Hao, D Zhanh. Additive manufacturing: a framework for implementation. Int. J. Production Economics 149 (2014) 194-201.

[7] W. Sutherland, S Bardsley, M. Clout, M Depledge, L Dicks, L Fellman, E. Fleishmann, D. Gibbons, B. Keim, F. Lickorish, C. Margerison, K. Monk, K. Norris, L. Peck, S. Prior, J. Scharlemann, M. Spalding, A. Watkison. A horizon scan of global conservation issues for 2013. Trends in Ecology and Evolution. 28 (2013) 1-22.

[8] Piazza, Merissa and Alexander, Serena, Additive Manufacturing: A Summary of the Literature"(2015). Urban Publications Paper 1319.

[9] S. Khajavi, J Partanen, J. Holmstrom. Additive manufacturing in the spare parts supply chain. Computers in Industry. 65 (2014) 50-63.

[10] Y. Huang, M. Leu, J. Mazumder, A. Donmez. Additive manufacturing: current state, future potential, gaps and needs, and recommendations. Transactions of the ASME. 137 (2015) 014001-014011.

[11] W. J. Sames, F. A. List, S. Pannala, R.R. Dehoff, S.S. Babu, The Metallurgy and Processing Science of Metal Additive Manufacturing, Int. Mat. Rev. (2016) 2016-2063.

[12] H. Gong, K. Rafi, H. Gu, S. Thomas, B. Stucker, Analysis of defect generation in Ti-6Al-4V parts made using powder bed fusion additive manufacturing processes, Addit. Manuf. 4 (2014) 87-98

[13] S. Yavari, S. Ahmadi, R. Wauthle, B. Pouran, J. Schrooten, H. Weinans, A. Zadpoor, Relationship between unit cell type and porosity and the fatigue behavior of selective laser melted meta-biomaterials, J. Mech. Behav. Biomed. Mater. 43 (2015) 91-100.

[14] Q. C. Liu, J. Elambasseril, S. Sun, M. Leary, M. Brandt, P. K. Sharp, The Effect of Manufacturing Defects on the fatigue Behavior of Ti-6Al-4V Specimens Fabricated Using Selective Laser Melting, Adv. Mat. Res. 891-892 (2014) 1519-1524.

[15] S. Everton, M. Hirsch, P. Stravroulakis, R. Leach, A. Clare, Review of *In situ* Process Monitoring and *In situ* Metrology for Metal Additive Manufacturing, Mat. And Des. 95 (2016) 431-445.

[16] H. Gong, K. Rafi, H. Gu, S. Thomas, B. Stucker. Influence of defects on mechanical properties of Ti-6Al-4Vcomponets produced by selective laser melting and electron beam melting. Materials and Design. 85 (2015) 545-554.

[17] L. Thijs, F. Verhaeghe, T. Craeghs, J. Van, J. Kruth, A study of the microstructural evolution during selective laser melting of Ti-6Al-4V, Acta Mater. 58 (9) (2010) 3303-3312.

[18] A. B. Spierings, M. Schneider. Comparison of density measurement techniques for additive manufacturing metallic parts. Rapid Prototyping Journal. 17 (2015) 380-386.

[19] W. W. Wits, S. Carmignato, F. Zanini, T. H. J. Vaneker, Porosity testing methods for the quality assessment of selective laser melted parts, CIRP Ann. Manuf. Technol. 65 (2016) 201-204.

[20] G. Tapia, A. Elwany, A review on process monitoring and control in metal-based additive manufacturing, J. Manuf. Sci. Eng. 136 (6) (2014) 60801–60811.

[21] W. Frazier, Metal Additive Manufacturing: a review, J. Mater. Eng. Perf. 23 (6) (2014) 1917-1928.

[22] T. Craeghs, S. Clijsters, E. Yasa, J.-P. Kruth, Online quality control of selective laser melting, 22nd International Solid Freeform Fabrication Symposium; Austin, TX, 2011.

[23] S. Kleszczynski, J. zur Jacobsmühlen, J. Sehrt, G. Witt, Error detection in laser beam melting systems by high resolution imaging, 23rd International Solid Freeform Fabrication Symposium; Austin, TX, 2012.

[24] J. zur Jacobsmühlen, S. Kleszczynski, D. Schneider, G. Witt, High Resolution Imaging for Inspection of Laser Beam Melting Systems, IEEE International

Instrumentation and Measurement Techonology Conference; Minneapolis, MN, 2013

[25] J. Mireles, S. Ridwan, P. Morton, A. Hinojoa, R. Wicker, Analysis and correction of defects within parts fabricated using powder bed fusion technology, Surf. Topogr.: Metrol. and Prop. 3 (2015).

[26] J. Schwerdtfeger, R.F. Singer, C. Körner, *In situ*flaw detection by IR-imaging during electron beam melting, Rapid Prototyp. J. 18 (4) (2012) 259–263.

[27] M. Aminzadeh, T. Kurfess, Layerwise Automated Visual Inspection in Laser Powder-Bed Additive Manufacturing, AMSE 2015 International Manufacturing Science and Engineering Conference; Charlotte, NC, 2015.

[28] EOSINT M 280. http://www.eos.info/systems_solutions/metal/systems_equipment/eos int_m280,

[29] B. K. Foster, E. W. Reutzel, A. R. Nassar, B. T. Hall, S. W. Brown, C. J. Dickman, Optical layerwise monitoring of powder bed fusion, Solid Freeform Fabrication Symposium Proceedings; Austin, TX, 2015.

[30] A. Jain. Data clustering: 50 years beyond K-means. Pattern Recognition Letters. 31 (2010) 651-666.

[31] K. Alsabti, S Ranka, V. Singh. An efficient k-means clustering algorithm. Electrical Engineering and Computer Science. 43 (1997).

[32] P. Matvkiewicz, J. Pestian, Effect of small sample size on text categorization with support vector machines, Proceedings of the 2012 Workshop on Biomedical Natural Language Processing; Montreal, Canada 2012.

[33] T. Howley, M. Madden. The genetic kernel support vector machine: description and evaluation. Artificial Intelligence Review. 24 (2005) 379-395.

[34] B. Waske, J. Benediktsson, Fusion of Support Vector Machines for Classification of Multisensor Data, IEEE Trans. of Geosci. and Remote Sens. 45 (2007) 3858-3866.

[35] M. Alonso, J. Malpica, A. Agirre. Consquences of the hughes phenomenon on some classification techniques. ASPRS 2011 Annual Conference. (2011).

[36] "Support Vector Machine." Wikipedia. Wikimedia Foundation, 21 Mar. 2017. Web. 03 Apr. 2017

[37] C. Cortes, V. Vapnik. Support-Vector Networks. Machine Learning. 20 (1995) 273-293.

Appendix A. CT and DSLR 3Images of an Anomaly Sample

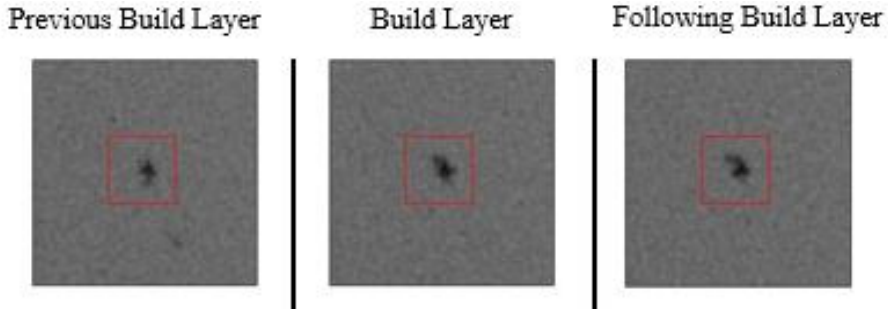

Figure A.1 CT images of anomaly sample with red outline representing feature extraction filter from DSLR domain

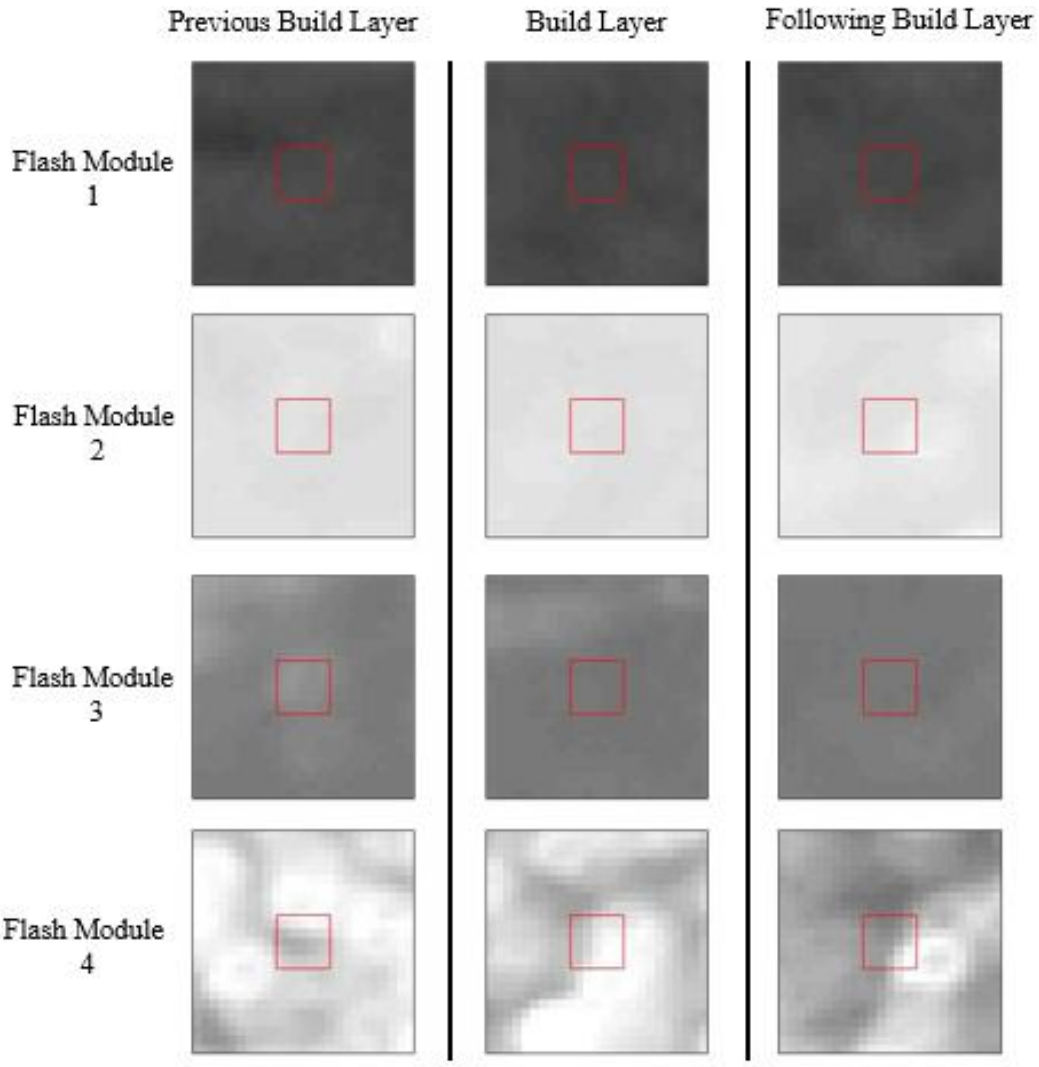

Figure A.2 Flash module 1-4 images of anomaly sample from previous, current and following build layer (depicted in figure A. 1) with outline of feature extraction filter in red.

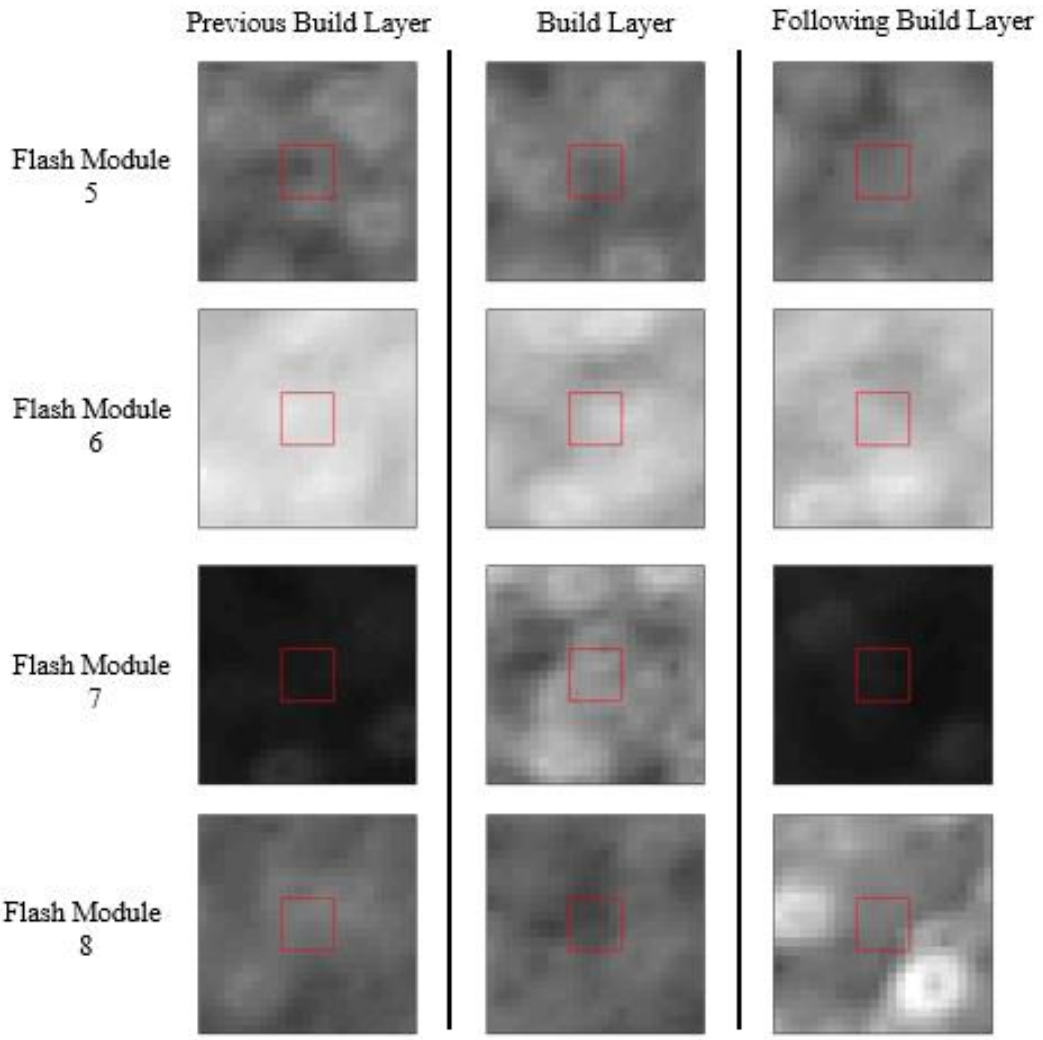

Figure A.3 Flash module 5-8 images of anomaly sample from previous, current and following build layer (depicted in figure A. 1) with outline of feature extraction filter in red.

Appendix B. CT and DSLR Images of a Nominal Sample

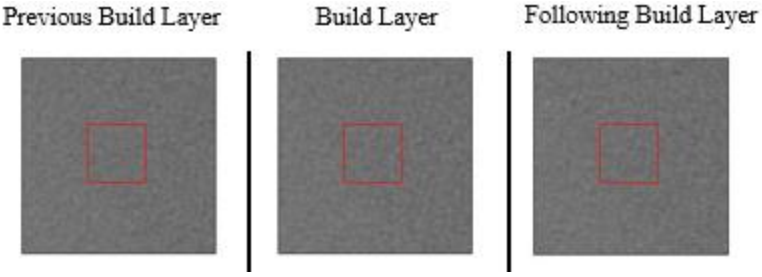

Figure B.1 CT images of nominal sample with red outline representing feature extraction filter from DSLR domain

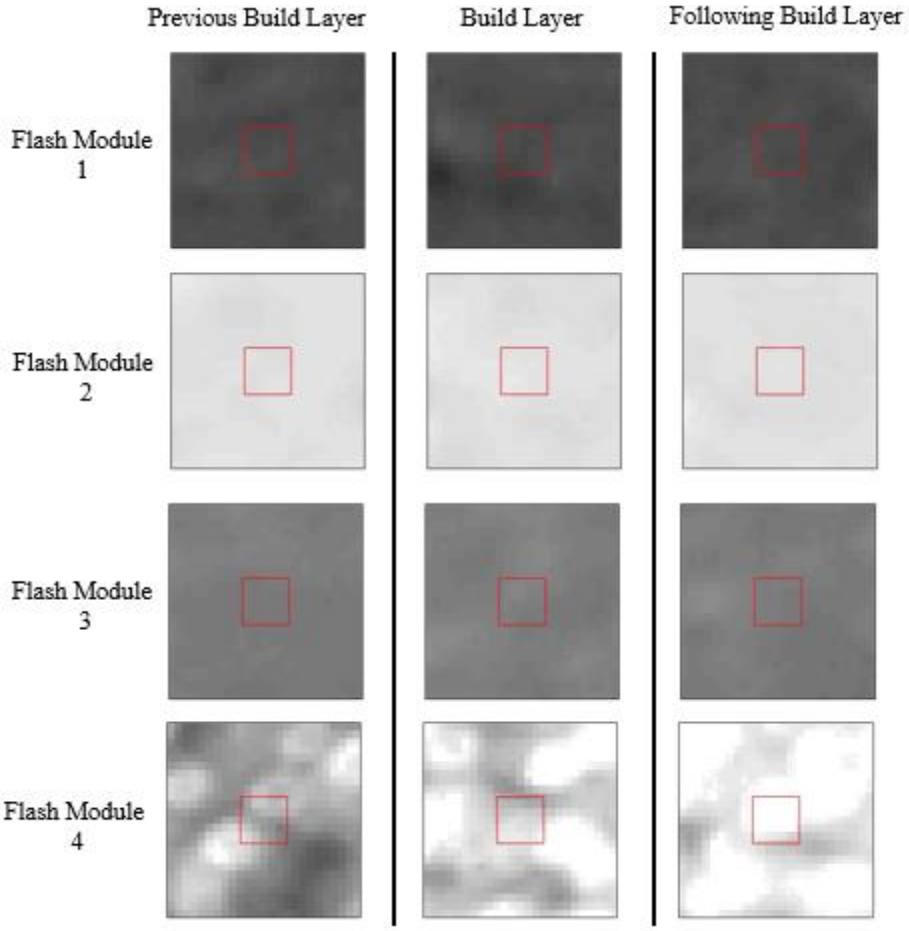

Figure B.2 Flash module 5-8 images of anomaly sample from previous, current and following build layer (depicted in figure B. 1) with outline of feature extraction filter in red.

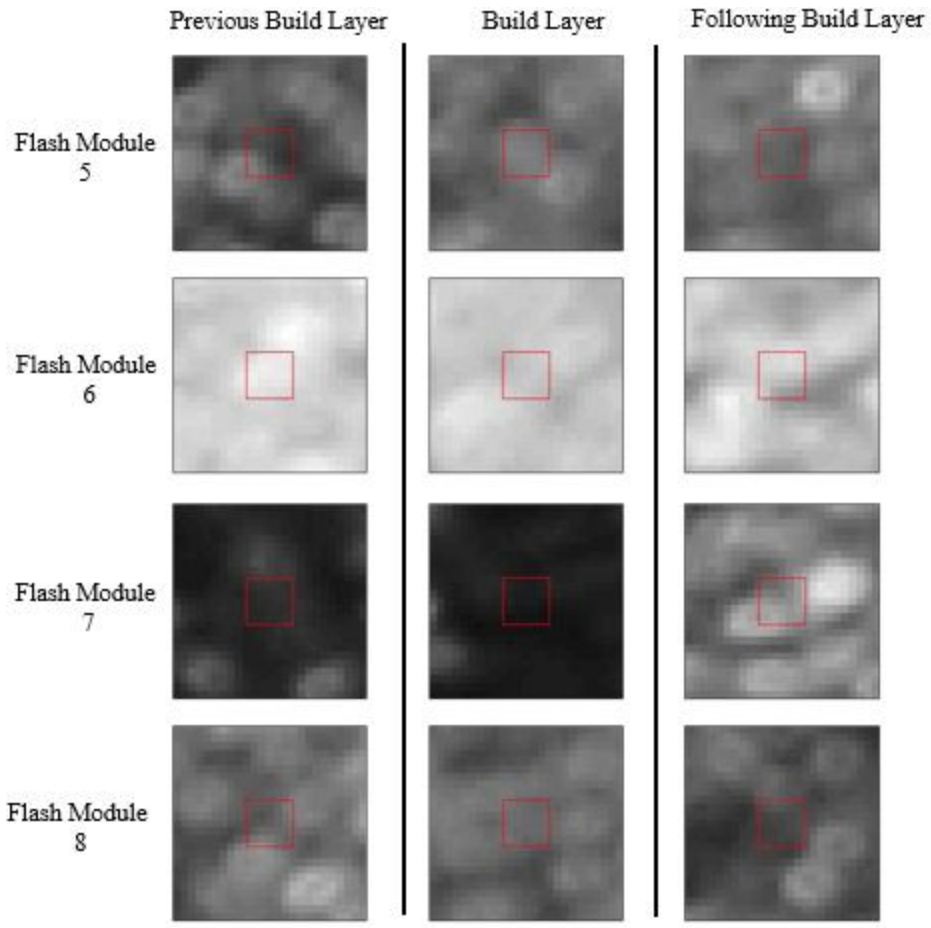

Figure B.3 Flash module 5-8 images of nominal sample from previous, current and following build layer (depicted in figure B.1) with outline of feature extraction filter in red.